Engineering Nucleic Acid Nanostructures for Sensing and Control of Biomolecules and Their Environments

A Dissertation
Presented to
The Academic Faculty

By
Victor Pan

In Partial Fulfillment
Of the Requirements for the Degree
Doctor of Philosophy in Biomedical Engineering

Georgia Institute of Technology, Emory University, Peking University
May 2020

Everybody wanna be a bodybuilder, but don’t nobody wanna lift this heavy-ass weight. Let’s go. I’ll do it though.
– Ronnie ‘The King’ Coleman

To Aibo, Yun-Long, Linda, Elsa, Fei-Fei, and Mars

ACKNOWLEDGEMENTS

First and foremost, I would like to thank my PhD advisor, Dr. Yonggang Ke, for his guidance and support through this entire process which not only included academia and my PhD, but opportunities and networking with labs in the nucleic acid nanotechnology field both in America and abroad.

To my doctoral committee, Yonggang Ke, Bryan Wei, Cheng Zhang, Khalid Salaita, and Zuhong Lu for their support throughout my adventurous, and international, PhD career.

I would like to thank members who were part of the Ke Lab, Salaita Lab, Lu Lab, Wei Lab, Zhang lab, and Myers Lab with whom I worked to complete my doctoral research work.

I would like to thank Shreyas Dahotre, and Dr. David Myers, who presented me with a unique opportunity to design and develop a technology that ultimately has become an integral component of my thesis. Their support and collaboration have been invaluable to my progress.

I would like to thank Dr. Muaz Rushdi, who was present in my PhD career every step

of the way. From my recruitment night, to my stay in Beijing, to becoming a close collaborator on one chapter of my thesis work. Without him, the entire course of my PhD would be very different.

I would like to thank Dr. Cheng Zhu for organizing and directing the joint BME-PKU program, which played an important role in my research.

I would like to thank my friends and co-workers at various labs in Beijing who selflessly spent countless hours helping me learn their techniques and technologies for application to my research: Dr. Taoli Ding, Dr. Wen Wang, Dr. Tanxi Bai.

Lastly, I would like to thank my friends who did not contribute to my thesis, but who have encouraged and supported me throughout this journey: Frank Hu, Dr. Charles Lin, Dr. Syed Faaiz Enam, Andrew Zhao, Natasha Fernandez Diaz Granados, David Wolfson, Victor Chong, Chris Rivera, Serik Tabarak, Kohei Sakurai, and Allie Lee.

Table of Contents

LIST OF FIGURES

LIST OF SYMBOLS AND ABBREVIATIONS

DNA: Deoxyribose Nucleic Acid

ssDNA: Single Stranded DNA

AFM: Atomic Force Microscopy

TEM: Transmission Electron Microscopy

TIRF: Total Internal Reflectance Microscopy

RICM: Reflective Interference Contrast Microscopy

UF: Uranyl Formate

TCR: T-Cell Receptor

MHC: Major Histocompatibility Complex

pMHC: Peptide-Major Histocompatibility Complex

STC: Surrogate T Cell

A2D2: Alive 2 Dead 2 streptavidin

Summary

Engineering Nucleic Acid Nanostructures for Sensing and Control of Biomolecules and Their Environments

By

Victor Pan

Doctor of Philosophy in Biomedical Engineering

Georgia Institute of Technology, Emory University, Peking University, 2020

Nucleic acid nanotechnology has emerged in the past decade as a powerful and versatile method to create functional and programmable nanostructures through molecular self-assembly. The research presented in this dissertation uses a specific nucleic acid assembly technique known as DNA Origami to create and apply designer DNA nanostructures to three separate biotechnology-related applications.

The first is a rigid fluorescent barcode system utilizing hierarchically assembled DNA origami nanorods, for use in situ labelling and detection of ssDNA and various proteins. Second, DNA origami is used to control the distance between two synergistic but non-interacting proteins to study their cooperative binding to a third protein. Finally, an adaptation of DNA origami is used to create a shear flow sensor capable of producing fluorescent signal in response to fluidic shear.

CHAPTER 1: Nucleic Acid Nanotechnology

In the central dogma, DNA's role is to store genetic information that, through transcription and translation, ultimately produces the proteins necessary for the biological function of all life. Contrary to this, the field of nucleic acid nanotechnology instead uses DNA as a building block material that can be designed and programmed to create physical nanostructures. This is possible for much of the same reason that DNA plays such a critical role to the propagation of life: it must be stable in a variety of solvents and conditions, it must be minimally toxic to cells, and most importantly it must behave predictably and consistently.

The details of how single stranded DNA hybridizes to form rigid and highly stable duplexes are outlined in Watson and Crick's Rules of Base Pairing [1]. The four nucleobases: adenine, thymine, guanine, and cytosine, are the basic building blocks of DNA. Through formation of hydrogen bonds, adenine binds with thymine while guanine binds to cytosine. These bases are connected sequentially by a phosphate backbone to form a single strand of DNA, and each strand of DNA is distinguished by the specific sequence of bases it contains. This single stranded DNA can then hybridize with a second single stranded DNA bearing a complementary sequence to form a double stranded duplex. Two strands of ssDNA without fully complementary sequences will be less thermodynamically capable of duplex formation. Given this, it is possible to rationally design and synthesize ssDNA that will hybridize with a DNA strand with arbitrary sequence.

After hybridization occurs, the ssDNA transforms from a freely jointed polymer chain to a significantly more rigid wormlike polymer chain [2]. This concept can then be scaled up such that one strand of ssDNA can contain several distinct domains of adjacent base pairs that respectively bind to different strands of ssDNA. The process in which this happens is an example of bottom-up molecular self-assembly, where separate components each adopt their thermodynamically favored conformations in relation to other components in the system to ultimately form stable supermolecular structures [3].

The most basic example of this is the Holliday Junction, which naturally occurs in biology during genetic recombination and double-strand break repair. Based on its structure, artificial Holliday Junctions have been created with asymmetrical unique domains such that they are migrationally immobile – unlike the Holliday Junctions in biological processes [4]. These rigid and migrationally immobile junctions are the basic building block of structural nucleic acid nanotechnology. By rationally designing many of these junctions to hybridize with each other, large and stable assemblies of DNA strands with specified shapes and dimensions have been created. The field has since advanced to employ more advanced building blocks and assembly methods such as various tiles, motifs, bricks, and lattices [5, 6].

DNA Origami

In a 2006 Nature publication, Paul Rothemund reported a technique for the assembly of large megadalton size DNA nanostructures with complex defined shapes and modifications [7]. This work represented a quantum leap in the possible complexity

and functionality of DNA structures. Previous techniques could only produce flat unbounded lattices or small basic objects with short single strands.

The name origami refers to the Japanese art of folding a sheet of paper into arbitrarily shaped objects. In DNA origami, the single stranded genome of the m13 bacteriophage (~7000 base pairs) is used as a DNA scaffold and is folded into a designed shape by hundreds of short synthetic DNA oligonucleotides. These short oligos, known as staples, are typically 20-60 base pairs long and each contain several domains that hybridize to portions of the scaffold DNA. During an annealing step of gradual temperature reduction over several hours, the staples hybridize to the scaffold and crosslink together spatially distant portions of the scaffold – essentially folding it into shape. This process of molecular self-assembly uses high temperatures to completely denature the scaffold and staples by inhibiting the DNA from adopting nonspecific secondary structures or aggregates. As the temperature is slowly decreased, the staples will begin hybridizing to the scaffold only once the melting temperature for a specific domain is passed. This method enables prioritization of thermodynamically favored sequences to hybridize, which in turn reduces off target or incomplete hybridization.

In Rothemund's first report of DNA origami, 2D planar objects of arbitrary shape with dimensions around 100 nm were constructed [8]. The next advancement in the DNA origami technique came in 2009 when Shih and coworkers bundled the DNA helices together in a honeycomb lattice to produce solid 3D structures [9]. Soon after, many groups reported new methods using the DNA origami platform to create objects of

ever-increasing complexity. Some of these ranged from circular gears, a nanovase, mosquito coil, and wire frame rabbit [10-18].

Functional Modification

One of the findings in Rothemund's original report of DNA origami was that the structures could be engineered to bear site-specific modifications. In his work, Rothemund added extra DNA at planned locations to write or draw simple images and text onto his structures which were then visible with AFM [8].

This is possible because each staple strand in the DNA origami is unique, and plays a specific role in crosslinking together domains of the scaffold that no other staple strands do. Therefore, each staple's location in the structure is known and unchanging. Then depending on where a modification is to be added, a staple at that location on the structure can be modified to contain a single stranded extension or handle that extends out of the origami and does not interact with the scaffold or any of the staples. A wide variety of functional molecules such as haptens, fluorophores, or antibodies can then be conjugated to a single stranded DNA complimentary to the extending handle protruding from the origami. In this manner, DNA origami offers fine and precise control of number of cargoes carried per nanostructure as well as their relative spatial arrangements.

This capability is what has made DNA origami such a valuable tool for studying nanoscale biological processes and interactions. No other technologies offer in situ control of molecule placement with resolutions down to just a few nanometers. With DNA nanotechnology, it now is possible to study many previously inaccessible fields

such as nanoparticle chirality affecting plasmonic resonance [19], ligand number and distribution on nanoparticle uptake into cells [20], and piconewton scale forces generated by living cells just to name a few [21].

To this end, the work presented in this dissertation showcases three applications where the unprecedented addressability and nanoscale control afforded by nucleic acid nanotechnology enables the systematic study and creation of new nanoscale tools. We demonstrate that the technologies described in this dissertation assemble as designed and function as intended.

CHAPTER 2: Verification Methods

While DNA nanotechnology enables precise design and engineering of functional nanostructures, it is important that the structures generated can be verified to be faithful to their planned phenotypes. The main tool to accomplish this task is agarose gel electrophoresis.

Agarose gel electrophoresis involves an agarose gel, the main component of agar, that is dissolved into buffer solution at various percentages by weight then allowed to gel. These gels become a 3D matrix of helical agarose in supercoiled bundles that contain pores and channels through which biomolecules can translocate, with gels of higher percentage of agarose having smaller pores. After an electric field is applied across the gel, charged molecules within the gel experience an electrophoretic force and migrate towards the oppositely charged electrode. It is the average size of these pores, and thus percentage of agarose by weight, that affects how quickly different sized biomolecules migrate through the gel. Higher percentage gels have greater resolving power of biomolecules with smaller molecular weight, and lower percentage gels are better for resolving larger species of interest. As full-size DNA origami are 5 megadaltons in size, they are considered relatively large biomolecules, and lower gel percentages are frequently used.

After the samples are run in the gel and product bands are stained and satisfactorily resolved, the band/s of interest are excised from the gel with help of a UV transilluminator. The isolated gel slices are mechanically crushed, then centrifuged to collect the purified liquid samples. The resulting DNA concentration is estimated with

Nanodrop UV/vis spectrophotometer, then the samples are ready for image verification or downstream applications.

Transmission Electron Microscopy

TEM is very frequently used to verify correct structure formation in three dimensional nanostructures. It works by illuminating the sample with a high voltage electron beam, commonly generated by a tungsten cathode filament. As the electrons pass through the sample, some are scattered. The electrons that successfully pass through the sample carry spatial information of the sample and are projected onto a phosphor screen for viewing. Electrons have a wavelength up to 100,000 times shorter than visible light photons, thus resolving power of this microscopy is immensely higher than traditional light microscopy – making this technique well suited for observing shapes and features in designed DNA nanostructures.

Samples are deposited onto carbon formvar grids and negatively stained with aqueous Uranyl formate, a heavy metal stain. The stain aggregates around the samples, forming a shell around the organic DNA structure. The stain around the vertical edges of the structure deflect more electrons than horizontal structure areas, allowing an outline of the DNA nanostructure to be clearly visible. However, as vertical edges are required for the UF stain to produce visible contrast of the sample, flat 2D structures such as one-layer shapes are difficult to image, and require a different form of microscopy for structural verification.

During imaging sessions, purified origami are examined for completeness and yield, as well as for other properties such as tendency to aggregate or mechanical flexibility.

A DNA origami design may produce a sharp band during agarose gel electrophoresis, but present consistent defects during imaging. This most commonly could be the result of impure starting materials or faulty design. Frequently, several rounds of trial and error might be needed before a design is deemed satisfactory. Consequently, it is extremely important to verify the robustness and fidelity of each design before proceeding with downstream applications.

In addition to assessment of origami structure quality, imaging microscopy is important for verification of added functional modifications. Handle extensions for capturing cargo produce identifiable minuscule migration shifts during gel electrophoresis, but verification of their correct placement and desired phenotype can only be confirmed with imaging. The single stranded extensions themselves are not visible with TEM, nor are many of the small molecule modifications that are commonly used such as biotin, digoxigenin, or fluorophores. On the other hand, larger modifications such as proteins and metallic nanoparticles are visible with TEM and can be routinely identified and have yields quantified. In some cases, it is even necessary to add proteins or metallic particles to a structure whose application does not require them, purely in order to account for the correct placement and expression of modifying handles.

Total Internal Reflectance Microscopy

There exist many forms of light microscopy, using visible light to illuminate and observe samples either directly or indirectly. Each of the different kinds of microscopy excel for specific applications and therefore specific sample types. In most of the light microscopy work described in this dissertation, the imaging modality best suited for the

task is TIRF, or Total Internal Reflectance Microscopy.

Total internal reflection refers to the complete reflection of a wave off the interface between two transparent media if the incident angle is sufficiently oblique. In the case of total internal reflectance, a phenomenon known as an evanescent field is produced opposite the interface off which light is reflecting. This evanescent field is a highly restricted electromagnetic field that decays exponentially in intensity with distance from the interface, and is the same wavelength of the incident light. This limits the area of excitation opposite the interface of reflectance to at most around a few hundred nanometers. Unlike other microscopy modalities that pass light directly through the specimen, TIRF selectively interrogates fluorophores in immediate proximity of the glass which produces enhanced signal to noise ratio with less light. This increases the clarity of the images as well as allows for less intense light sources to be used, which prolong fluorophore longevity by reducing bleaching. Overall, this form of microscopy is excellent for fluorescent DNA origami imaging due to the application's single molecule nature and preference for selective imaging in close proximity to glass.

CHAPTER 3: Rigid Fluorescent Barcodes Hierarchically Assembled from DNA Origami Nanostructures

A barcode is a widely used technology for labelling items that are to be quickly distinguished and identified. First developed in 1951 and used to categorize railroad cars, the barcode experienced commercial success in 1973 when it was adopted to automate supermarket checkout systems. Since then, they have become commonplace in our lives – with a 2D version called a QR code even being used to identify social media and bank accounts on personal devices.

In biomedical science, a very primitive version of barcodes has long been used for identification of biological components. By employing different color fluorophores or dyes coupled to a targeting peptides or antibodies, different cellular components could be stained and identified. However, there are only a few categories of spectrally distinguishable fluorophores, which greatly limits the number of unique biomolecules that can be tagged in a single imaging sample. While this has been satisfactory for decades of research, some applications are now calling for methods of multiplexed detection for more efficient sample analysis.

Many methods of multiplexed fluorescent identification of disparate biological entities have been developed in recent years. Some examples of these utilize technologies ranging from fluorescent polymers to quantum dots to structural DNA nanotechnology. Of these, barcode systems created with DNA nanotechnology have stood out as versatile platforms capable of tagging many unique biomolecules in a variety of applications.

The nature of structural DNA nanotechnology, governed by the predictability and reliability of Watson-Crick base pairing, allows for many unique barcodes to be constructed with great consistency [7]. Over the years, this field has produced many remarkable methods with strategies that are mRNA based, dendrimer based, and m13 scaffold based just to name a few [22-24]. While these technologies have successfully advanced the current capability of creating more and more unique barcodes, they are all heavily dependent on using multiple spectrally distinguishable fluorophores to generate the bulk of their resolvable combinations. Necessitating many fluorophores for barcode construction is more expensive, complex and requires more sophisticated imaging equipment. In addition, reduced dependence on fluorophores for barcode construction leaves some colors available for labelling other biological components in situ.

The goal of this chapter is to create a barcode system that is less dependent on multiple different colored fluorophores. Another goal is to take advantage of a sub field in DNA nanotechnology, Hierarchical Assembly, to make larger rigid barcodes capable of being imaged with less specialized microscopes. Hierarchical assembly is the practice of using completed structures as building blocks to create even larger structures. Instead of constructing these structures entirely with unique components, the bulk of the DNA strands are conserved, drastically reducing cost and labor of manufacture. Only a small portion of the strands, used to connect the larger DNA structures needs to be designed and purchased.

Barcode Design

The first step towards these goals was to choose a building block for HA that would fit the needs of the barcodes we wanted to design. The barcodes would need to be long enough to support several on/off bits, all while allowing for each bit to be spaced far enough apart such that each is spectrally resolvable. Another consideration is that the persistence length of this structure should be sufficiently straight such that several of them linked end to end would still exhibit minimal bending, which could hinder the ability of the barcode to be identified. Finally, we wanted the system to be easily customizable to create all different combinations with fewer staple mixes.

Given these considerations, we selected the DNA origami 10 helix bundle nanorod for its increased persistence length over previously published DNA nanostructure barcodes [25]. Conveniently, the 10 HB nanorod has an overall length of about 250 nanometers, approximately the threshold of diffraction limited microscopy. This would mean a single 10HB nanorod is long enough to allow for two fluorescent 10 HB nanorods on either side to be resolvable as two separate dots. From there, the number of possible bits per barcode is limited by the number of nanorods that can be

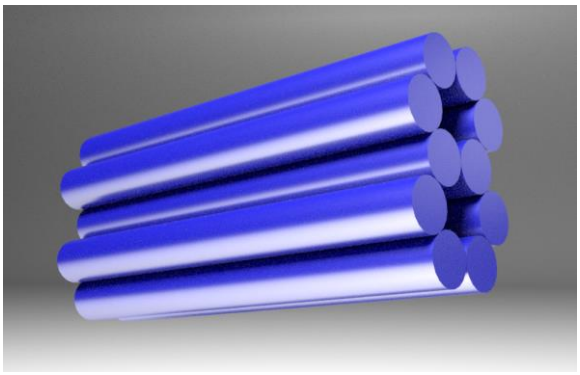

Figure 1 *– Cartoon of 10HB nanorod featuring its helix organization and double-barrel structure.*

hierarchically assembled together and purified with reasonable yield.

First, it was necessary to design the 10HB to be fit for HA. The hex lattice 10HB has been published before [26], but was used for a different application and would not be suitable for stable hierarchical assembly. To address this, a custom version of this structure had to be designed – with focus primarily on the nanorod's two ends.

The ends are especially important because geometry of the helices on the tail of the nanorod must fit into the geometry of the head helices so that the two structures don't kink or bend when joined together.

The other complication in designing this structural unit is that the head of the next unit cannot simply be attached to the tail of the first unit, due to polarity mismatches in the sticky ends. Possible solutions included flipping every other unit, offsetting the helices (only possible in square lattice designs), or rotating the structure 180 degrees along its long axis. We found that the last proposition could be employed by designing the nanorod to be radially symmetrical, which allows for polarities to match while maintaining proper geometrical fitting of each structure into the next. Although this creates a 180 degree flip of the fluorophores on each successive monomer unit, no functional difference or effect could be observed during fluorescence imaging.

With planned monomer unit that theoretically would suffice for hierarchical assembly, caDNAno was used to design the structure to fit this plan [27].

In addition to fulfilling the requirements for HA, the scaffold of this structure was routed to increase overall versatility by featuring a plethora of functional modifications sites. The structure consists of 17 repeating bands of 10 staples, 8 of which have both 5' and

3’ end located at outer positions. The other two staples have both ends located towards the inside of the nanorod, and thus are not able to bear handles for capture of functional DNA. This means for each band of 10 staples, there are a possible 16 locations for addition of cargo-capturing handles, or 272 per 10HB nanorod. While the vast majority of these won’t be used at any given time, the customizability of this structure for different applications is high.

As each 10 HB nanorod structure is a standalone DNA origami construct, a method was needed to connect multiple nanorods together to achieve hierarchical assembly. Traditionally, this was accomplished with sticky ends, single stranded extensions that hybridize with complimentary sticky ends on a different structure. If the 10 HB was to be connected end to end to make a long 1-dimensional wire-like superstructure, sticky ends would have to be designed on either end of each monomer. Given that the structure is 10 bundles of double stranded DNA, a single stranded extension could be added to each helix bundle, to result in 10 sticky ends on each end. Using as many sticky ends as possible increases specificity and stability. Collaborators in the Wei Lab have optimized HA protocols for multiple DNA origami structures, and settled on 10 base pair sticky ends as the most efficient design.

Preliminary Assembly Experiments

Using tried and true protocols for DNA origami samples, we assembled and analyzed the 10HB monomer structure with agarose gel electrophoresis. TEM imaging of the excised bands was used to verify the monomer structures. Next, preliminary HA of the 10HB monomer was tested by using two sets of sticky ends that allowed the monomers

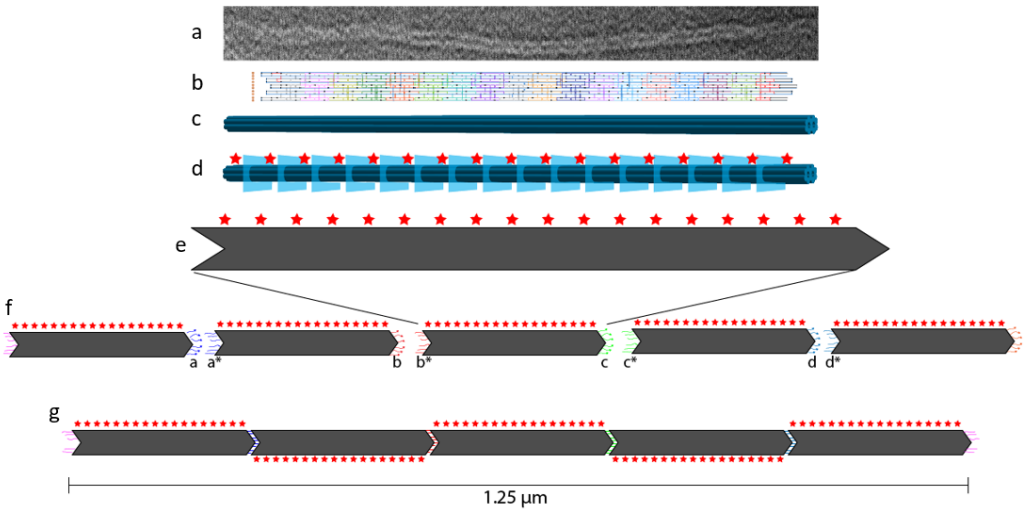

Figure 2 *– TEM image of 10HB nanorod (a). caDNAno design showcasing 17 repeating bands of staples (b). Helix bundle cartoon (c). One fluorophore is added to each of the 17 repeating bands of staples for a total of 17 fluorophores along a single monomer to create an 'on' bit. Simplified cartoon of 'on' bit (e). 5 connected 'on' bits showcase the axial flipping from one monomer to the next to allow for sticky end polarity to match (g).*

to connect end-to-end indefinitely. Monomer 1 and Monomer 2 were assembled separately with their respective sticky ends, then combined and concentrated with 100k MWCO spin columns used to remove any excess staples. With a protocol for fusion of the distinct monomer samples adopted from other HA work in the Wei lab, samples were incubated at a gradient of temperatures to choose the condition that produced the highest yield. A 15-hour isothermal incubation at 42C and a gradual step down to room temperature was the chosen protocol for yield. TEM images of this unpurified sample revealed long continuous wires with little branching and aggregation. The wires had minimal kinks or obvious joint misalignment suggesting the sticky end mediated connection between separate monomers was seamless.

Assembly of Controlled-Length DNA Barcodes

Next, multiple sets of sticky ends were designed so end to end assemblies of 10HB

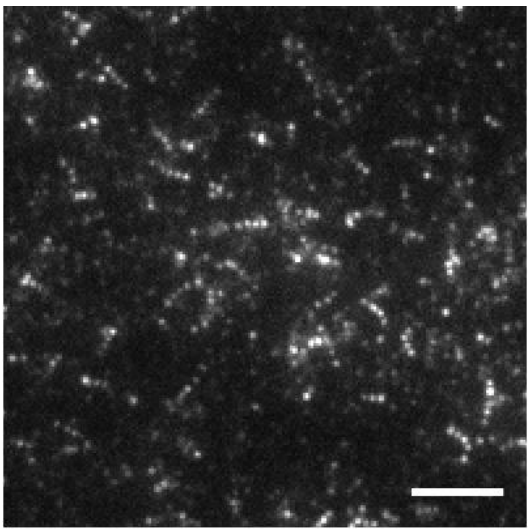

Figure 3 *–TIRF imaging of unpurified 1010101010 10-mer. Individual resolvable spots are visible along with some structures bearing the designed 5 spots. However there is much nonspecific fluorescence and the image is replete with incomplete structures. Scale bar 2.5 microns.*

structures with defined length could be created. We also designed a set of staples with extensions for capturing fluorescently modified DNA strands. We used Alexa 488 for its robust quantum yield and its resilience to bleaching. To make the entire monomer fluorescent, one modified handle was added to each of the 17 repeating bands of staples – creating a row of fluorophores running along the entire length of the monomer. This monomer would be an “on” bit; likewise, a monomer with no fluorescence would be the off bit. First, we attempted to form a 1010101010 10-mer structure with total length approximately 2.5 microns, the same assembly protocol as the linear growth sample was used except this time 10 unique monomer samples had to be constructed first instead of two. In preliminary imaging experiments, unpurified samples were diluted then deposited onto uncleaned glass. Using TIRF, long fluorescent structures with resolvable and approximately equally spaced dots were noted among many spots

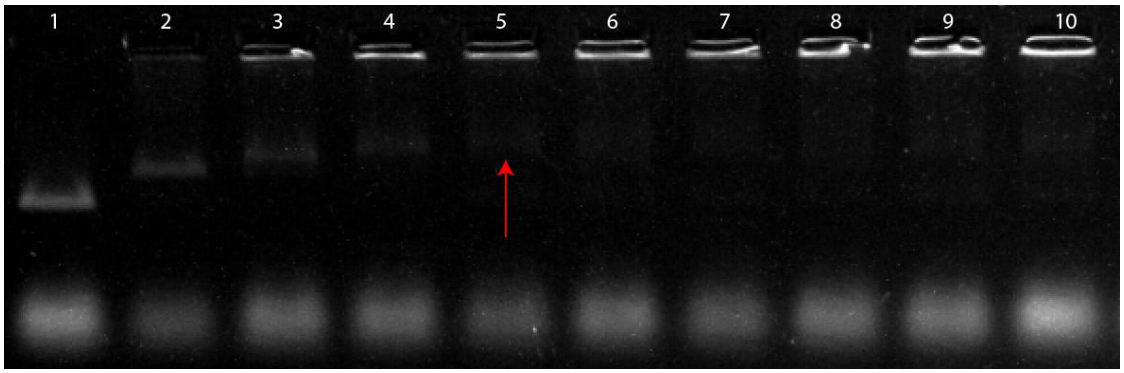

Figure 4 *– Agarose gel electrophoresis of hierarchically assembled barcodes with gradually increasing length. The monomer lane (far left) can be clearly seen with no visible aggregates in the well. As more 10HB nanorods are connected, product band mobility decreases in both intensity and mobility. 5 assembled monomers produces a faint but clear band.*

of nonspecific fluorescence. Although the images were very dirty, we verified the feasibility of imaging these barcodes.

After modifying the structure with biotin strands, biotinylated bovine serum albumin was coated onto plasma cleaned glass, washed with blocking buffer, covered with streptavidin, and washed again. Finally unpurified DNA samples were added and then washed after a short incubation at room temperature. We envisioned that this washing step could reduce incomplete structures that remained on the glass as everything without a biotinylated extension should theoretically be removed. The plasma cleaning of the glass and extra washing improved image clarity greatly – we also discovered using ultrapure filtered buffers could reduce the amount of background fluorescence.

Assembly Method Optimization

With an improved method of imaging, we tried to devise a more robust method of sample preparation as the current method could produce incomplete barcodes that were indistinguishable from complete products post-washing. For example, a 1010101010 where only 8 components with including first block (which contains the

biotin groups) would remain attached to glass and would look like 10101010 which is an entirely different barcode combination. We first attempted to establish the largest linear HA structure that could be directly purified with AGE. Our results showed that a 5-mer produced a band, although faint, that could be reliably excised and purified (**Figure 4**). Anything larger aggregated into wells and was not feasible for AGE purification. Therefore, we found that a 5 + 5 addition system where two 5-mers were gel purified then subsequently fused into a 10-mer produced a higher yield of complete barcodes. Additionally, unfused 5-mers would either get washed away or be easily distinguishable as incomplete.

Additional 10-mer Purification Attempts

Amidst our attempts to establish a better method for 10-mer assembly, we attempted some methods for 10-mer purification. Noting that 5-mer could be purified with AGE, we hypothesized that reducing the percentage of agarose in the gel would allow for larger constructs to enter the gel instead of becoming trapped in the wells. From the already lower-than-usual agarose percentage of 0.7% for 5-mer purification, we reduced the agarose gel concentration to as low as 0.2%. In conclusion we found that no matter how low the agarose gel concentration was lowered, a band for the completed 10-mer would not form. Random portions of the lane were excised and imaged anyway, and some stray 10-mers were found. This revealed that 10-mer barcodes were in fact able to run into the gel, but not in a uniform manner that produced a concentrated band of product that could be purified. After TEM imaging of unpurified 5 and 10-mer products, we saw completed products along with large aggregates – with

more aggregates in the 10-mer barcodes. This suggested that longer barcodes with more unique monomers had increased formation of aggregates, thus reducing the yield of non-aggregated fully formed barcodes that could run into the gel and be purified by band excision. This could be due to all the free sticky ends during the fusion incubation step. If random sticky ends displace sticky ends from a properly assembled monomer, the monomer may no longer hybridize to the monomers it is designed to hybridize to. Subsequently we attempted first purifying the monomers before assembly, but this likewise resulted in poor yields. To better understand how the sticky ends interact during the fusion step, more research needs to be conducted.

Dot and Dash Barcoding

With 5 + 5 assembly selected as the best method, we created a wide variety of 10-mers with different combinations of ‘on’ and ‘off’ bits, and noticed that one ‘on’ bit could be distinguished from two consecutive ‘on’ bits as the latter would not be spectrally resolvable and thus look like a short dash instead of a single dot. This could be extended by increasing the number of consecutive on bits to increase the length of the dash. Realizing that this is the simplest form of shape-based barcoding, we sought to create a full set of 5mers using this dot-and-dash concept showing every possible combination.

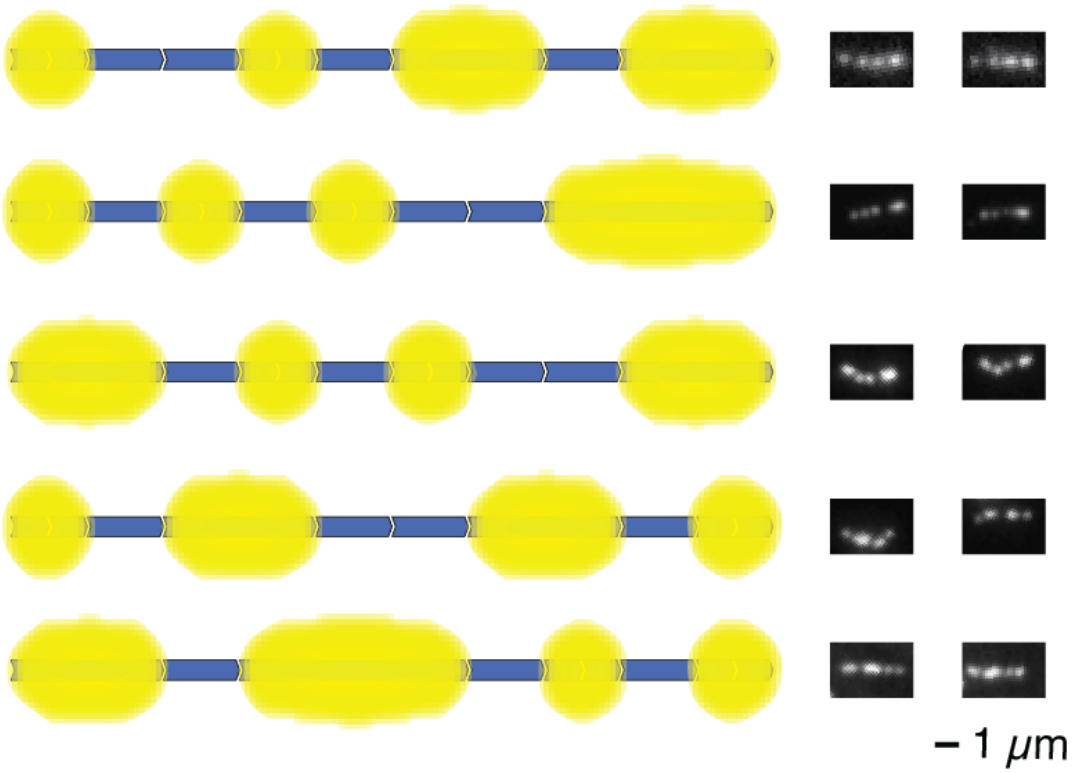

Figure 5 *– Agarose gel electrophoresis of hierarchically assembled barcodes with gradually increasing length. The monomer lane (far left) can be clearly seen with no visible aggregates in the well. As more 10HB nanorods are connected, product band mobility decreases in both intensity and mobility. 5 assembled monomers produces a faint but clear band.*

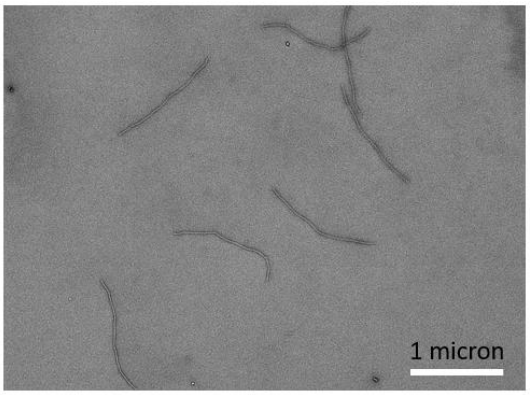

Figure 6 *–TEM imaging of gel purified 5-mers.*

5-mer Barcode Combinations

Current art with three resolvable spots in a single spectral color can produce 4 combinations, while our method can produce 13. As the barcodes are 5-mers, they were assembled with previously described protocols, and purified with AGE. TEM imaging reveals uniform length and good monodispersity (**Figure 6**).

Super Resolution Imaging

Expanding on the goal of producing more combinations with a single color, we demonstrated a few more strategies that may be more suitable for certain applications. One of which is that our design can be modified to support super resolution imaging.

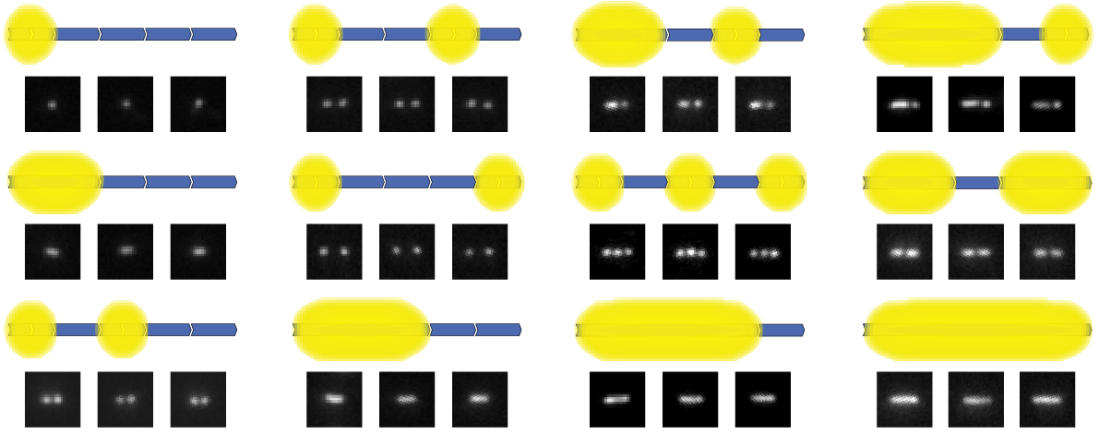

Figure 7 *–Representative TIRF imaging of gel purified 5-mer barcode combinations.*

Instead of a single row of fluorophores along the entire nanorod, we concentrated fluorescent handles into bands of the repeating staples. Although each band is capable of capturing 16 fluorescently modified DNA strands, we started with only 8 fluorophores per band – one per staple instead of two so the staples were not too long. After trying a 10101 barcode with a single fluorescent band for each ‘on’ bit, we confirmed that 8 fluorophores was enough to create a consistent and clear signal during imaging. With the significantly improved resolution of super-resolution fluorescence microscopy at 50 nm and below compared to 250 nm of diffraction limited microscopy, having several fluorescent ‘on’ bits on a single 10HB nanorod was possible. Using the bands 3/9/15 to carry 8 fluorophores each with each band spaced 60 nm apart, a single monomer could now express three bits of information.

Using this modified structure, we applied STORM super resolution imaging to this barcode system. A 5-mer barcode made using the 3-band on bit presents 15 possible bits. Alexa 647 was used for its blinking properties which are necessary for this form of imaging. We demonstrated the versatility of this platform by performing information encoding with Morse Code to write the three letters D, N, and A. The three-band

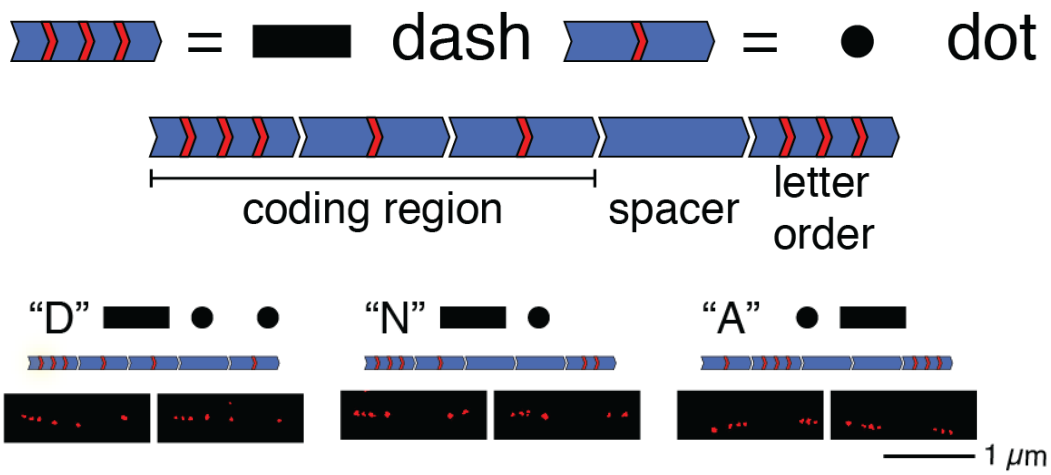

Figure 8 *– Using three fluorescent spots on a single monomer as a dash, one spot as a dot, and the last monomer to indicate letter order, simple messages in Morse Code can be decoded in a single imaging session.*

origami represents a dash while the single band origami depicts a dot. The three barcodes were prepared separately then mixed together and imaged in a single session. Each 5-mer barcode allocates three of the DNA origami structures as the letter encoding region, followed by a spacer and final set of bits depicting letter order. This way, all information regarding letter identity and order is contained within the sample which allows all information to be decoded in a single imaging session.

Multi-color Capability

While our technology was primarily designed to be and presented as a single-color system, we still showed its capability for multi-color imaging. Using only a single color, a barcode with five bits is only capable of 13 combinations because the ends are not distinguishable. Without the capability to establish barcode polarity, the majority of 2^5 combinations such as 10100/01010/00101 are not distinguishable from each other. However, by adding a second color, polarity can be determined which allows the

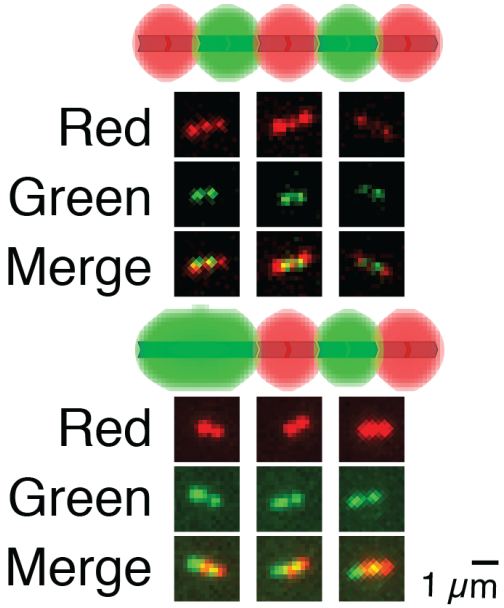

Figure 9 *– Barcodes carrying multiple colors increase the total number of possible combinations by allowing for end identification.*

number of combinations from one color to be increased from 13 to 32. Then the second color can also be used to make multiple combinations independent of the first color. However, the second color is still constrained by symmetry, so the total possible barcode combinations is less than 13*32. Further, only 4 unique staple mixes need to be prepared for such multiplexing capability: no color, first color, second color, and both colors.

Combing and Barcode Alignment

The issue of barcode symmetry could be addressed with another method, one that does not require the use of a second color. The strategy for doing this lies in devising a method to distinguish one end from the other, as the barcodes deposit onto the glass in random orientation. In the first publication of DNA origami barcodes, the three spots

were spaced apart asymmetrically – allowing visual consistent visual confirmation of which end is which. However, in our design that seeks to drastically reduce the number of unique staple mixes that must be prepared, asymmetrical spacing cannot be used. Instead we found that the structures can be combed into a single direction such that each barcode's single anchor point would be upstream of the combing direction with the free end downstream. As even repeated unidirectional washing was not producing any alignment, we attempted to do this with several methods such as molten agarose injection, isopropyl alcohol flushing, and centrifugation. Eventually we discovered that combing could be achieved by blasting nitrogen through the tape microfluidic. Doing so would create high enough surface shear stresses to overcome any charge-mediated attachment of barcodes to glass, and align the barcodes in the direction of fluidic flow. This method was risky because improper funneling of gas through the microfluidic could displace the coverslip from the tape and completely ruin the sample. Also, an unfortunate side effect was that all buffer would have to be ejected from the chamber, so fluorophores during imaging quench much faster. Additionally, incorrect alignment of the gas applicator with the fluidic resulted in turbulent gas flow, which aligned the barcodes more haphazardly.

Buffer Mediated control of Barcodes on Glass

As work with this project progressed, we discovered that the barcode's charge mediate adhesion to glass could be controlled by varying buffer salt concentrations and pH. The barcodes are purified in a 0.5x TBE 10 mM Mg2+ buffer, and adding even 25% volume of PBS removed all binding of barcodes from the glass. Also, running buffer

that has become too acidic (pH <8) no longer facilitates barcode binding. In order to have the strongest adhesion, a “sticking buffer” consisting of pH 9 running buffer without any sodium was used. Contrary to the sticking buffer, a “lifting buffer” consisting of pH 7.4 PBS was used. We discovered that barcodes attached to glass at one end via biotin/streptavidin or digoxigenin/anti-digoxigenin in the “lifting buffer” would exhibit a bound end, with the rest of the barcode flailing around through Brownian motion. However, the “sticking buffer” could be applied and the barcodes would then fully adhere to the glass and be clearly visible. Subsequently, the “lifting buffer” could be

Figure 10 *– Barcodes 10101, 11010, and 11000, combed using buffer exchange.*

added again to reverse the binding effect. We hypothesize this pronounced effect can be attributed to the hydroxylation of the glass surface caused by plasma cleaning. Increasing the pH could result in deprotonation of the hydroxyl groups on the glass, increasing the glass's negative charge. More negatively charged glass would interact more with the divalent magnesium cations that form a bridge of charge interaction with the origami.

One of the takeaways of buffer mediated control of barcode to glass adhesion is that combing could now be performed with a much more repeatable and controlled method that preserved fluorophore stability. The barcodes would be deposited onto glass in the lifting buffer. Following a short incubation to allow for hapten conjugation, the fluidic is washed with lifting buffer to remove any unbound DNA, then again with sticking buffer to adsorb the barcodes to the glass. During this process, the barcodes are pushed down to the surface of the glass in the direction of flow and combed. If the combing process is completed before the barcodes are physisorbed, significantly less shear is required.

Additional Combination Generation Methods

Following our experiments with super-resolution imaging of up to three fluorescent bands on a single 10HB nanorod, we noticed that regular diffraction limited imaging of these same structures yielded varying fluorescent intensities. We created some barcodes with 'on' bits of 3 different fluorescent intensity – 1, 2, or 3, fluorescent bands. TIRF imaging of a hybrid barcode with each of the different intensity values shows visibly different fluorescent intensity on each barcode. While there is apparent variation

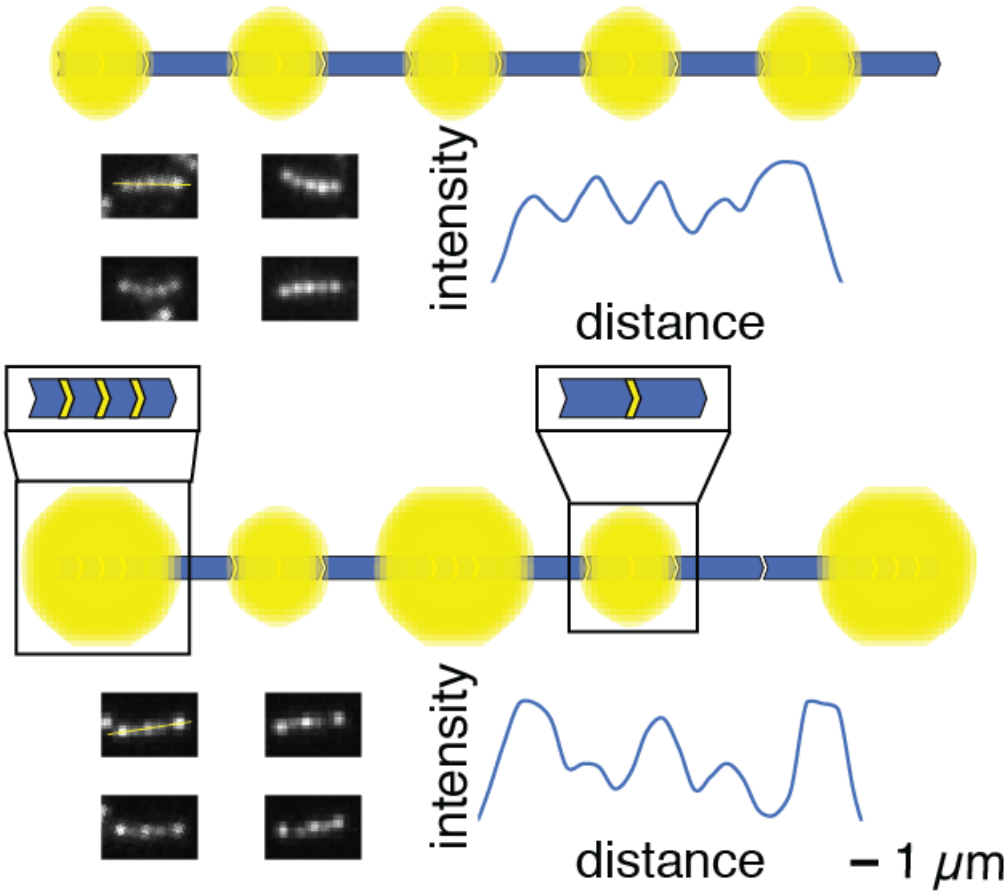

Figure 11 *– Barcodes with 'on' bits consisting of different numbers of fluorescent bands produce varying levels of fluorescence..*

in bits on some of the barcodes, we believe this to be a potential method to create more combinations with a single color.

Protein Capture

To demonstrate the versatility of this fluorescent barcode system, we showed its use in capturing and identifying biomolecules in a variety of settings. First, a 5-mer barcode with combination 10001 was outfitted with extensions that bear capture strands for mutated Cas9 proteins. After the barcodes were adhered to the microscope coverslip, Cas9 proteins and guide RNA were added. TIRF imaging after a short incubation showed the proteins (labelled with a different color) colocalized on the entirety of the

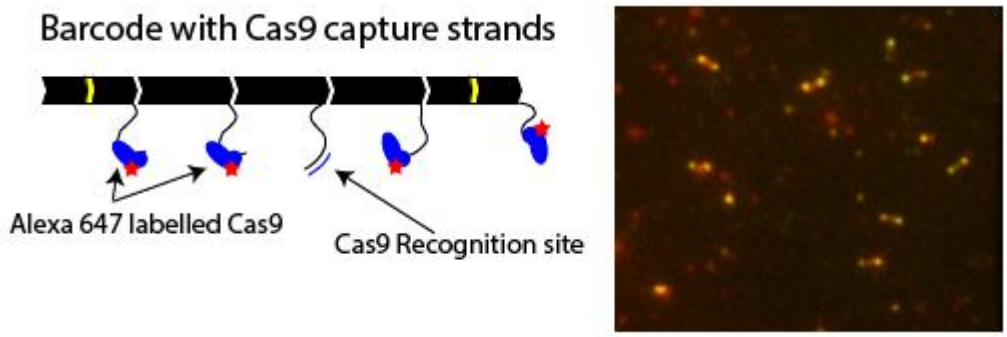

Figure 12 *– Barcodes demonstrating capture and colocalization of fluorescent Cas9.*

barcode (**Figure 12**). By using a different color for the proteins their presence on the barcodes could be directly visualized, which would not be possible in a system that needs all spectrally distinguishable fluorescent colors to create barcode combinations. Next we applied a 10-mer barcode with a single fluorescent spot to a DNA curtain setup. DNA curtains are long rolling circle amplification products that are tethered to a lipid coated glass surface, and extended past a barrier such that they are all lined up uniformly (**Figure 13**). One of the major issues facing DNA barcode systems is that the DNA must either be double stranded or extended with some sort of ssDNA binding protein. DNA barcodes, being already rigid in nature, easily extend on the curtain barrier setup. However, the specific curtain setup used for demonstration of the

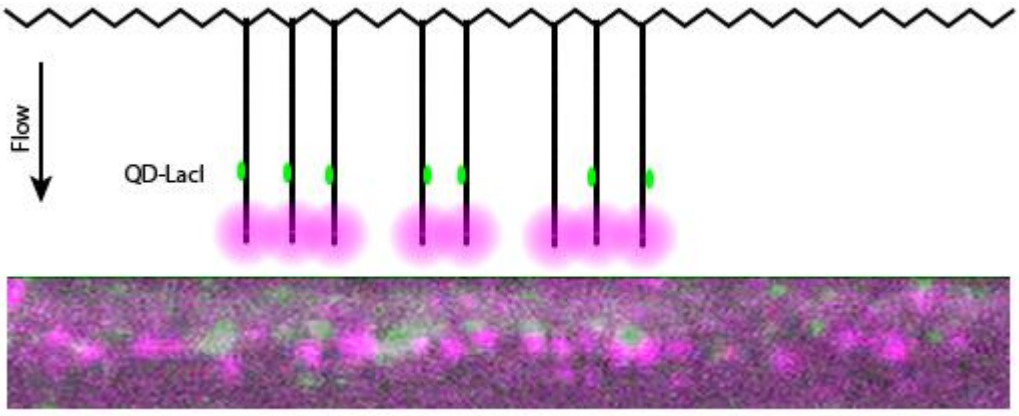

Figure 13 *– DNA curtain capture of 10-mer barcodes exhibiting QD-LacI capture.*

barcodes was created for DNA curtains 30k bases long, so the imaging resolution is low. Even with a 10-mer barcode, very limited number of combinations could be made so we used the simplest barcode for concept demonstration– a single on bit. Extensions for the capture of LacI protein were added to the barcodes in known location. Following capture and alignment of the barcodes downstream of the barrier, quantum dot labelled LacI protein was added to the chamber and incubated briefly. The presence of LacI could be confirmed, as green dots were seen in the expected position along the curtain slightly above the line of pink dots.

DNA Target Capture

Next we used the barcodes to detect synthetic DNA target strands. A sandwich hybridization method was implemented where the target oligonucleotide was used to connect the barcode to a biotin strand. Successful sandwiching resulted in a barcode that could attach to the streptavidin coated glass. Without the correct target strand, the barcodes could not capture a biotin strand and would thus be washed away. We simultaneously tested 5 barcodes which each were specific to a unique target strand, but all had an identical domain for the same biotin strand. We found that of a mixture of the 5 barcodes, only ones corresponding to the added target strand could be visualized in TIRF. Our first experiments with this application showed some nonspecific binding of untargeted barcodes to glass, but following our establishment of sticking and lifting buffers, washing has been more effective and nonspecific binding decreased. Successful demonstration of this concept indicates this technology's potential application as an end-user friendly multiplexed nucleic acid target detection system.

Conclusion

In summary, we used DNA origami and hierarchical assembly to present an adaptive and versatile barcoding system with less dependence on spectrally distinguishable fluorophores. Our system is modular in nature and doesn’t require many different staple mixes for each combination. While the 5-mer barcodes can be reliably assembled, any larger barcodes require an extra fusion step and have a final purity of only 50 percent. A more robust purification procedure still needs to be developed, especially for longer barcodes.

CHAPTER 4: DNA-Origami-Controlled Intermolecular Spacing Tunes Binding Cooperativity

Surface receptor engagement of ligands between cells initiates intracellular signaling cascades culminating in cellular function and fate comprising immune recognition of pathogens, and cell development and differentiation. T cells, for instance, are programmed to recognize foreign antigens over the course of an infection and in response, extensively proliferate in order to mount a robust clearance of the specific foreign entity. The programming and immune clearance is centered around the T cell receptor (TCR) recognition of a unique peptide anchored within a groove of the invariable major histocompatibility complex (MHC, or pMHC when including the peptide) presented on the surface of an antigen presenting cell. Their binding results in intracellular phosphorylation of adjacent CD3 proteins which initiates a signaling cascade toward T cell activation. One approach to studying binding between TCR and pMHC is surface plasmon resonance which has resulted comprehensive kinetic measurements of affinity, and on- and off-rates between various TCR-pMHC pairs [28]. Another approach is to use single force spectroscopy methods such as the micropipette adhesion frequency assay (MAF) or biomembrane force probe (BFP) which closely mimics the two-dimensional junction whereby the surface anchored receptor-ligand pair will engage [29]. We have previously demonstrated that affinity and on-rate measurements made using MAF correlate well with T cell effector function, supporting the importance of maintaining the two-dimensional cell junction environment. Using single force spectroscopy, we have also found that coreceptors expressed on T cells can simultaneously engage with pMHC along with TCR, in a

fashion that is synergistic to otherwise bimolecular binding. T cell coreceptors are thought to facilitate the initiation of the intracellular signaling cascade by recruiting kinases and therefore play a critical role in the sensitivity of immune recognition and T cell activation, but their engagement to MHC has been difficult to characterize due to their low affinity. In particular, the CD4 coreceptor engagement to MHC has been notoriously elusive to detection due to its presumed remarkably low affinity. Thus, the general consensus for the function of CD4 is to not enhance bond formation between TCR and pMHC, but to recruit kinases for CD3 phosphorylation [30]. Further characterizing coreceptor interactions will more clearly define their role in regulating homeostasis and initiation of immune responses.

Crystal structures of protein complexes reveal docking geometry and localization of precise patches by which proteins interact by hydrogen bonds and noncovalent interactions [31]. Elegant gain-of-function mutations on the CD4 coreceptor afforded spontaneous crystal formation between the TCR, pMHC, and CD4, enabling observation of their complexing. Fascinatingly, the rigid coreceptor maintains a membrane proximal spacing of roughly 7 nm apart from the TCR while binding to the MHC, possibly providing an adequate gap for CD3 proteins to amalgamate around the TCR. Such localization hinges on an interaction between both the intracellular portions of the proteins- which has been recently studied- and the extracellular portions which has been elusive. Importantly, the formation of crystals suggests that the specific geometric docking represents an energetically favorable orientation and restricting the individual protein components as such may minimize the energy required to form a

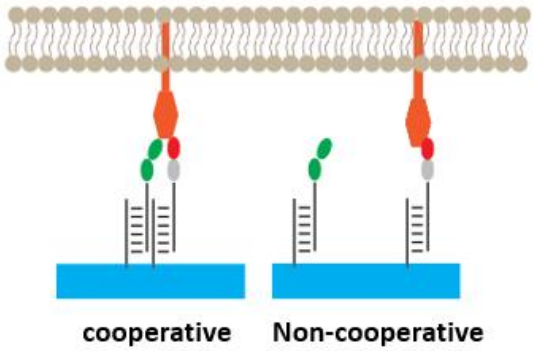

Figure 14 – CD4 (green) and TCR (red) spaced too far apart cannot exhibit cooperative binding, but are expected to cooperatively bind to a third protein (MHC – orange) if placed close enough together.

trimolecular complex. To corroborate these findings using wild-type CD4, we sought to control the distance between TCR and CD4 in order to determine if a critical distance exists such that cooperative binding is supported.

As previously explained in this dissertation, DNA nanotechnology has emerged as a groundbreaking paradigm for the creation of nanoscale tools and devices with programmable features. Capable of fabricating large megadalton scale DNA constructs in complex custom shapes with addressable features, we deemed DNA origami to be well-suited to address the question at hand. Knowing the dimensions of a designed nanostructure, we modified individual staple strands to bear extensions at locations of interest, so the nanostructure could be enabled with multiple functional capabilities.

Recent work demonstrated that DNA origami can support mechanical forces for integrin-RGD interactions that far surpass peak loads TCR-pMHC interactions can experience [32]. This work serves as a foundation for using DNA origami to conjugate

proteins on cell-mimicking surfaces which can be probed against one another.

DNA-origami nanostructures were loaded onto surrogate cell surfaces and used to multiplex two synergistic but non-interacting molecules. We confirmed protein multiplexing on these DNA origami with TEM imaging and flow cytometry, and also that the surrogate cell surfaces were coated with DNA origami. We then used the micropipette adhesion frequency (MAF) assay to measure bond formation between the three molecules as TCR and CD4 were differentially spaced apart. Measurements of bond stiffness by biomembrane force probe (BFP) served as corroborating evidence that these molecules are synergistic. We revealed a critical distance and the extent to which bond synergy can occur.

DNA Origami Design

In deciding what structure would be suitable for this application, we concluded it should be a rod-like structure to have increased real-estate to host a variety of distances. Also, we first wanted to study linear distance variation and not 2D arrays of proteins. Next the structure needed to be straight such that it did not have propensity to curve and distort the designed protein distance. Given these criteria and that we previously designed a 10 HB nanorod to be versatile, 1D, and straight, we chose to use the 10 HB for this work. However instead of expressing handles to capture fluorescently labelled DNA oligos, handles for origami attachment to the surrogate T-cell and protein conjugation would be needed. Another convenience of this structure is that its double-barrel phenotype could have a clear upper and lower face. We chose one face and covered the entire length of the structure with 19 handle extensions for surrogate T-

cell attachment. On the opposite face, we chose and modified 5 strands with extensions. The first modified extension was located near the middle of the structure and would be used to capture CD4. The other 4 strands all bore a conserved sequence at varying distances away from the first modified extension. Distances were calculated from the point at which the handle extension exits the structure. We chose four

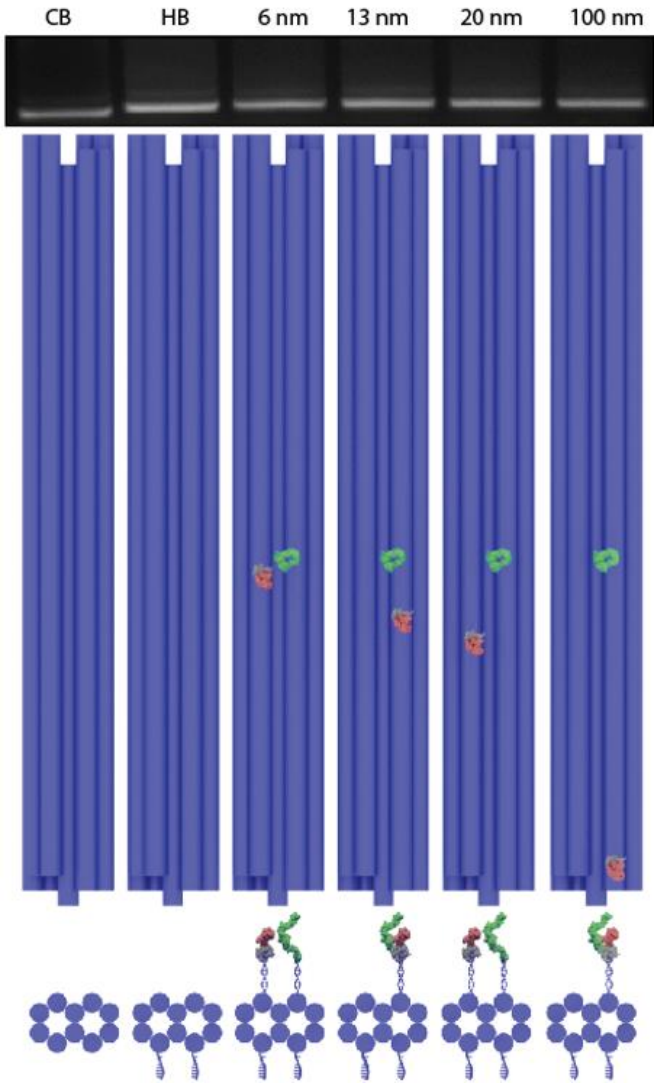

Figure 15 – Agarose gel electrophoresis of two blank controls and four protein spacing conditions. Agarose gels were run prior to protein loading, and reflect mobility of origami and handles only. Protein models are added to depict location of handle extensions.

distances: 6, 13, 20, and 100 nanometers. While we already expected the 20 nm distance to exhibit no synergistic binding, we included the 100 nm distance as a negative control.

We used these modified strands and created 4 staple mixes, each with the first modified strand and one of the other 4 distances to have two protein capture extensions either 6, 13, 20, or 100 nanometers apart. To verify correct design of these modified structures, each of the four versions was equipped with a biotinylated strand at both protein extensions, annealed, and purified via agarose gel electrophoresis. **Figure 15** depicts clean band formation with the Complete Blank sample exhibiting fastest gel mobility. Handle Blank sample has 19 extra handles on its bottom side, and thus has slightly slower mobility. The 4 protein spacing distances each have two more extensions than the HB sample but have same total extensions relative to each other. This results in their indistinguishable mobility being slightly slower than the HB sample. TEM imaging was performed after the purified samples were loaded with streptavidin and blinded by a colleague. By examining the resulting apparent distances between the two streptavidin molecules, the identities of the four blinded samples were correctly

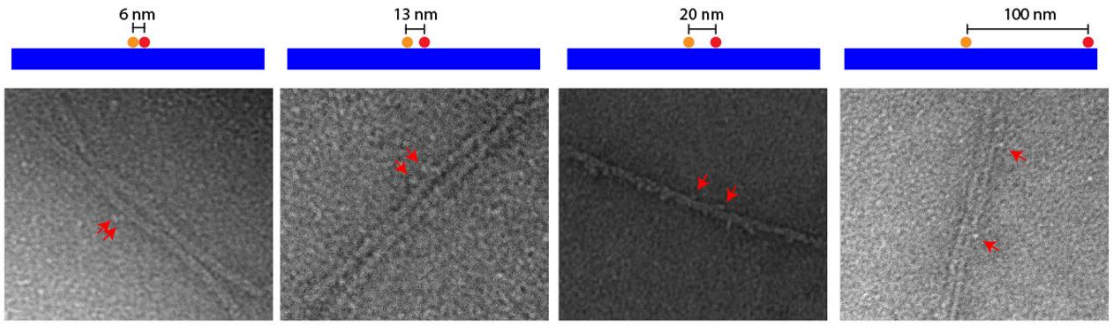

Figure 16 – TEM images of DNA origami nanorods demonstrating streptavidin spacing at different designed distances. Distances 6, 13, and 100 nanometers show dimerized origami. 20 nanometers is non dimerized, but contains streptavidin along the bottom.

divined.

Surrogate T Cell (STC) Preparation and Optimization

With verification of origami fidelity and functionality, we began efforts to assemble surrogate T-cells. Our first surrogate T-cell candidates were red blood cells. These cells had biotinylation on random surface proteins, and were coated in streptavidin. The 19 extensions on the bottom of the 10HB origami were used to capture DNA strands modified with a terminal biotin group. Origami bearing these bottom extensions as well as two handles differentially spaced CD4 and TCR were annealed and purified, then incubated on separate batches of streptavidin coated RBCs. Next, biotin-streptavidin conjugation was again used to add both proteins onto the origami. Because of this redundancy, both proteins could not be added at the same time. First one of the unique biotinylated strands had to be added, then washed, then incubated with the first biotinylated protein. After another wash to remove excess protein 1, the second biotinylated strand was then added, washed, incubated with the second biotinylated protein, then washed again. This was an incredibly labor intense process that resulted in poor yields of completed surrogate T cell RBCs with both proteins added.

Flow Cytometry STC Quality Control

After the STC preparation process was completed, fractions of the various STCs were stained with mouse anti-human TCR Cβ PE conjugated antibody or mouse anti-human

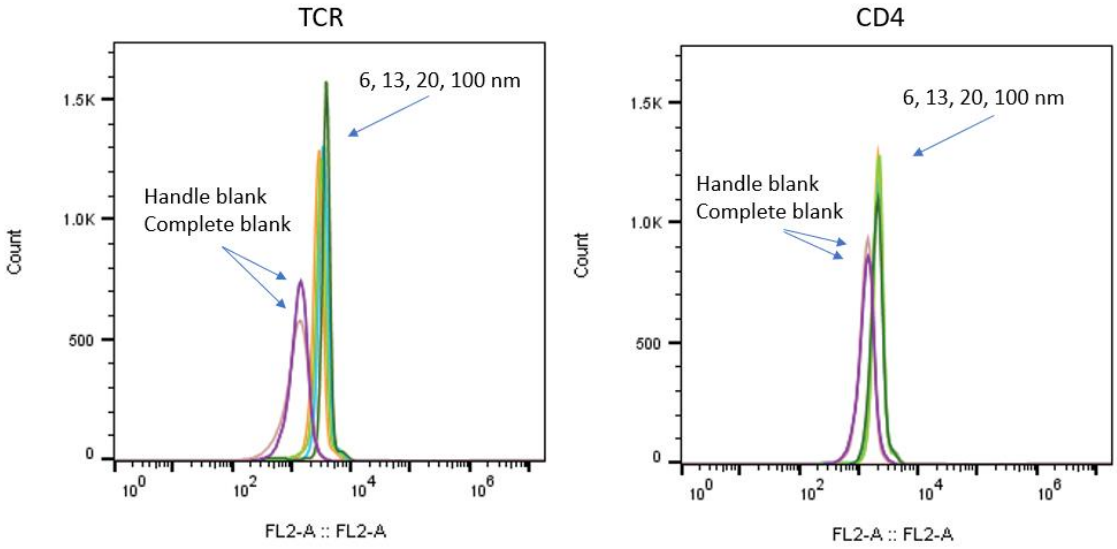

Figure 17 *– For flow cytometry verification of both TCR and CD4 staining on prepared surrogate T Cells, both blanks show baseline fluorescence while all four distances have consistent, sharp peaks at almost the exact same fluorescence levels.*

CD4 PE conjugated antibody (**Figure 17**). Site densities of each protein on the origami coated beads were quantified by calibrating their fluorescence intensities against PE calibration beads. Staining of both proteins for flow cytometry verification of their presence on the surrogate T cells produced inconsistent results from experiment to experiment, and there was too much nonspecific binding between the surrogate T cell and RBC covered with pMHC. For each experiment, two controls were prepared: one with handles for surrogate T cell attachment but no handles for protein attachment (Handle Blank or HB), and an origami with no handles at all (Complete Blank or CB). Both negative controls showed significant binding to the pMHC coated RBC.

Reducing Nonspecific Binding Events

Due to unacceptable levels of nonspecific adhesion and too many simultaneous uses of biotin-streptavidin conjugation, we switched to polyT beads to utilize DNA hybridization for origami attachment instead. Doing this would reduce one of the biotin-streptavidin implementations, and was not reliant on the surface proteins of the RBC which likely contributed to the nonspecific binding. These beads, magnetic beads known as Dynabeads, are commercially available and meant for purification of mammalian mRNA from genomic DNA. They come ready-to-use pre-coated with single stranded 30 bp dT DNA that hybridizes to the poly A tail on mRNA. Instead of a biotinylated strand being hybridized to the bottom 19 origami extensions, a strand with 30 dA tail was used instead. This enabled attachment of the origami onto the beads with a simple incubation in salted buffer, where the dA extensions on the origami would hybridize with the dT extensions on the beads. Using agarose gel electrophoresis, we ensured that this method could result in origami loading onto the beads.

Agarose Gel Band Depletion Assay

Two dT coated bead sizes were used for testing: 3 μm and 12 μm in diameter. Equal quantities of purified DNA origami were loaded onto each of the beads for an hour, and only beads with the fully modified extensions for surrogate t-cell mounting showed reduction of the origami band – indicating the origami has been sequestered by the beads which are too large to run into the agarose gel. With the 3 micron beads showing cleaner origami capture, and also being a more manageable size for MAF assay, we chose to proceed with the 3 micron beads.

The amount of purified DNA origami added to the beads in the experiment above was purposefully less than how much was used historically – the rationale for this was to ensure a depletion of the band intensity would be visibly apparent. With the gel for 3-micron beads revealing an almost complete disappearance of the origami band, we erroneously assumed that the reduced amount of origami added was in fact the beads' total origami capacity. This resulted in flow cytometry verification of the loaded surrogate T-cells to have very low staining for both proteins. In response to this, we tested loading with incrementally increasing amounts of purified DNA origami, but noticed that the leftover depleted bands as the DNA amount increased were only slightly increasing in intensity. This confirmed that the on-rate of origami onto the bead is dependent on origami concentration, and that the bead capacity indeed was greater than what we thought it was. Expanding upon this, we repeated the experiment with an overnight incubation instead of one hour, and saw almost complete depletion of all

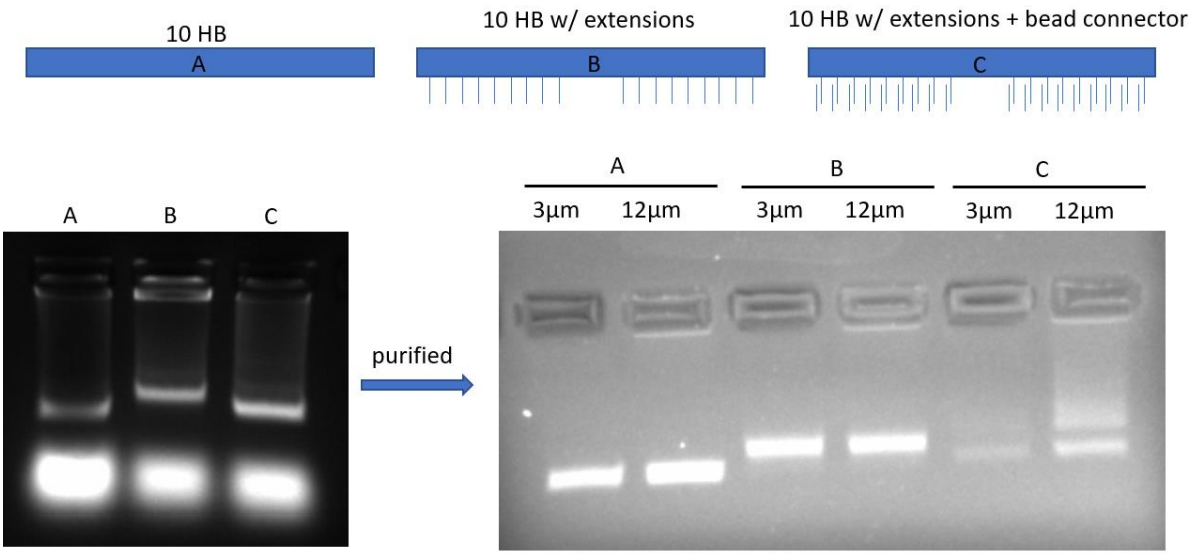

Figure 18 *– Only origami that have the bead connector strands hybridized with the extensions show loading onto the dT coated beads.*

DNA origami added (**Figure 19**). Only the last lane of the DNA amounts (250 ng) tested showed an appreciable leftover band, but knowing the origami on-rate is dependent on concentration, we hypothesized that true saturation of the beads with origami required even higher amounts of purified DNA origami. To confirm this, we tested overnight loading onto beads with 250, 500, 750, and 1000 ng of DNA origami, and verified with before and after Nanodrop UV/vis spectrophotometry that the saturated capacity of the beads is about 400 ng for 15 uL of the Dynabeads. Henceforth, we conducted every bead-loading step with at least 1000 nanograms of each origami sample to ensure the beads were always saturated.

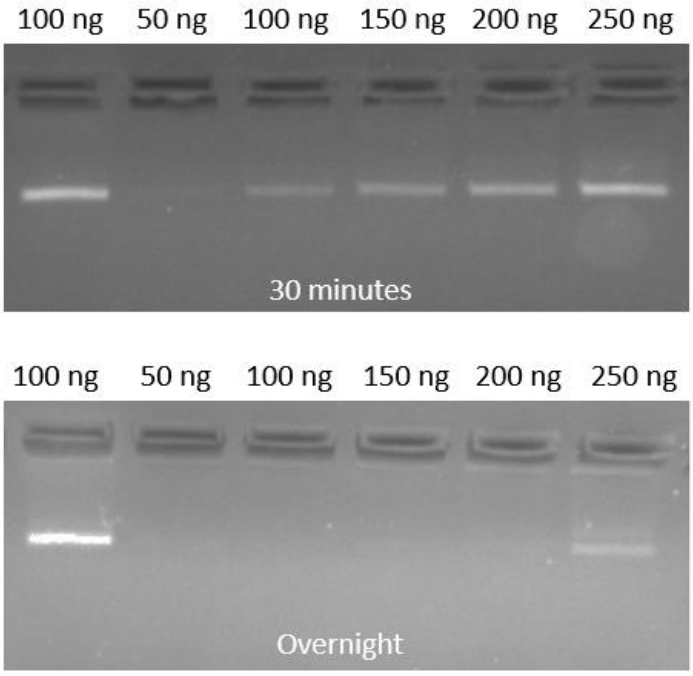

Figure 19 *– Origami loading onto dT beads is concentration dependent, while overnight incubation allows for better saturation of bead surface with origami. Band intensity in the gels show leftover origami, with no band indicating all origami has been sequestered by the beads. Left most 100 ng lanes incubated without beads to serve as controls.*

Blocking of Nonspecific Binding to Bead with dA Blocking Strand

Next, we had suspicions that beads fully covered with single stranded dT DNA would have nonspecific binding to the pMHC-RBC. Even if the beads were fully loaded with DNA origami, due the Origami's high aspect ratio, we suspected that there would be

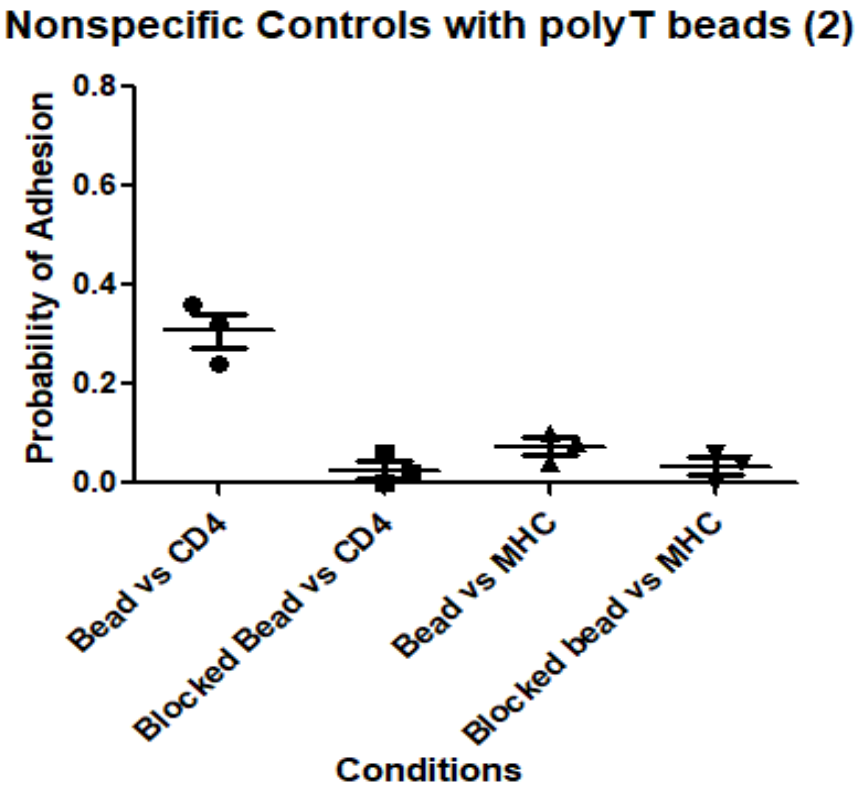

Figure 20 *– Unloaded poly-T beads probed against CD4 coated red blood cells demonstrate significant adhesion. Blocking the beads with high concentration of poly-A ssDNA drastically reduces nonspecific adhesion.*

regions of exposed dT DNA handles that could be hotspots for nonspecific binding. To address this issue, we prepared a 25 dA blocking strand that could hybridize with the bead's single stranded extensions to make them double stranded. Double stranded DNA, unlike single stranded DNA, does not have as many free sites for hydrogen bonding. It is also worth noting that the blocking strand, 25 dA, can block the majority

of each 30 dT bead extension. However, as the handles located on the bottom of the origami contain 30 dA, displacement of the origami from the bead is thermodynamically unfavorable. Therefore, these blocking strands could be added in large excess after saturation of the bead with origami to block any remaining unbound dT extensions.

We tested blocked and unblocked beads against RBC coated with various proteins and noted significant reduction in nonspecific binding with the blocked beads. Testing the surrogate T-cell loaded with origami also showed very low nonspecific binding, as the origami is fully double stranded.

With our initial concerns of nonspecific binding addressed, we proceeded to continue optimization of protein loading onto the surrogate T-cells. Both proteins were still being attached to the origami with biotin streptavidin interactions, which required extra wash steps and enabled possible crosstalk between the streptavidin proteins at closer distances (6 and 13 nm). Additionally, for attachment of proteins to origami, we used A2D2 streptavidin, or mutated streptavidin with only two active sites. We hypothesized that this mutated streptavidin would establish a more specific 1:1 ratio of protein to streptavidin.

CD4 Conjugation to DNA

The preliminary MAF assay was performed multiple times with inconsistent flow cytometry verification of the surrogate T cells as well as nonsensical adhesion frequency results. This was attributed to the complexity of STC preparation so we sought to simplify and streamline the process by conjugating one of the proteins to a DNA strand that replaced one of the biotin streptavidin interactions. This way, both

proteins could now be added simultaneously instead of sequentially, and all attachment steps in the STC assembly process would use unique chemistries.

Solulink® protein to DNA conjugation kit was used for the conjugation, and conjugated product was purified with FPLC and verified with SDS-PAGE. The SDS-PAGE gel shows the initial CD4 protein and the successfully conjugated product, which depict a disappearance of the initial band and presence of several new bands representing the protein with increasing numbers of conjugated DNA. Following our adoption of this new method of attaching CD4 to the STC, flow cytometry verification of the CD4 protein yielded increased with more consistent experiment-to-experiment fluorescence. MAF assays performed with this updated protocol were more streamlined, but adhesion frequency data regarding protein spacing was still inconsistent with our expectations. From here, we hypothesized that the A2D2 mutated streptavidin was the issue. While the A2D2 streptavidin was verified to contain only two active sites, which sites were active on each protein is not known. Given the tetrahedral geometry of streptavidin, this results approximately half of the proteins with two adjacent active sites. In this

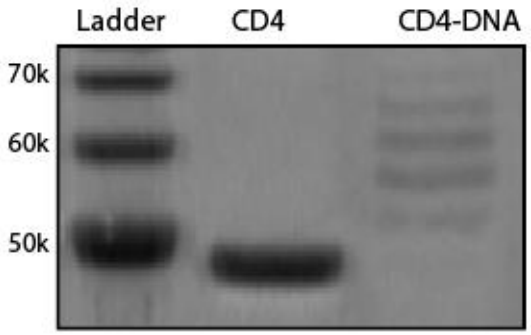

Figure 21 *– SDS-PAGE of CD4 conjugated to linker DNA for attachment onto DNA origami.*

case, steric hindrance would make simultaneous binding to the biotinylated DNA strand and biotinylated pMHC difficult.

Once A2D2 streptavidin was replaced with wild type streptavidin, flow cytometry verification of TCR attachment to the STC likewise improved and became more consistent. While we did consider that using wild type streptavidin would allow for more than one TCR to bind to each streptavidin, which would inflate TCR counts and undermine the single-molecule aspect of this experiment, TEM imaging showed this case was extremely rare.

Considering that we had great results with conjugating CD4 to a DNA strand, this was not possible with the TCR due to its custom nature. This TCR was supplied by a

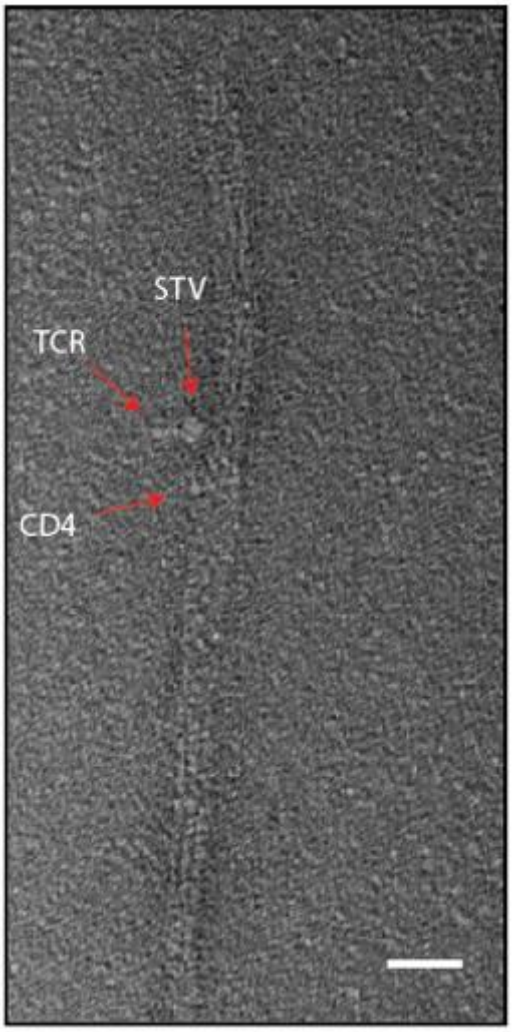

Figure 22 *– TEM imaging of 10HB nanorod with 20 nanometer protein spacing. CD4 can be seen in the correct location closer to the center of the nanorod. Approximately 20 nanometers away two proteins are visible. Scale bar 20 µm*

collaborator, and being a double chained protein, was not stable enough to endure the various chemical reactions and washes necessary for the conjugation process.

With finalized methods of protein attachment to origami, we used TEM to verify the completed origami assembly and loading with CD4, TCR, and STV. This imaging was difficult to perform, as its procedure differs from the that of loading onto the surrogate T cell. Unlike the STC which can be washed to remove excess proteins during the

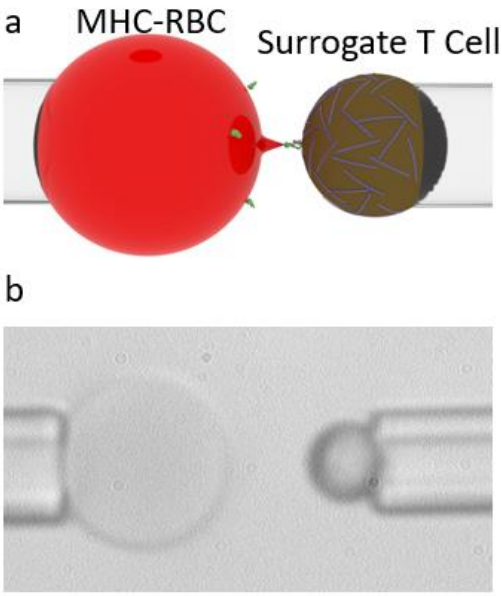

Figure 23 *– Schematic and representative brightfield image of MAF assay.*

stepwise STV and TCR attachments, free origami cannot. This meant the origami and proteins had to be imaged unpurified, which would clog up the images with nonspecific proteins. However in addition to our flow data, we were able to find and confirm proper assembly of the origami and all three proteins as designed.

Optimized Micropipette Adhesion Frequency (MAF) Assay

Surrogate T cells were probed against pMHC coated RBC using MAF. In this assay, aspirated pMHC-RBC and STC were repetitively brought into contact with one another

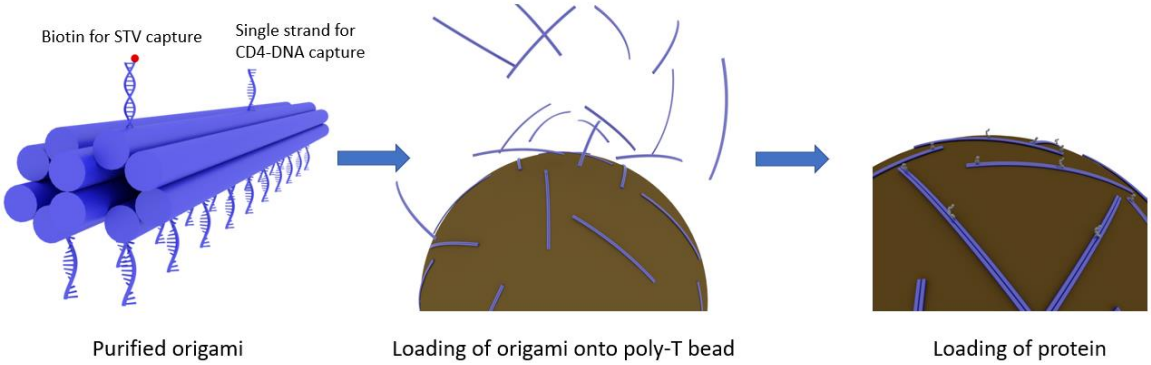

Figure 24 *– Agarose gel purified origami are loaded onto poly-T magnetic beads overnight. After unbound origami is washed away, proteins are added in high concentration then washed away. Next the beads are blocked with 25 dA blocking strand, then washed again before flow cytometry verification of protein loading.*

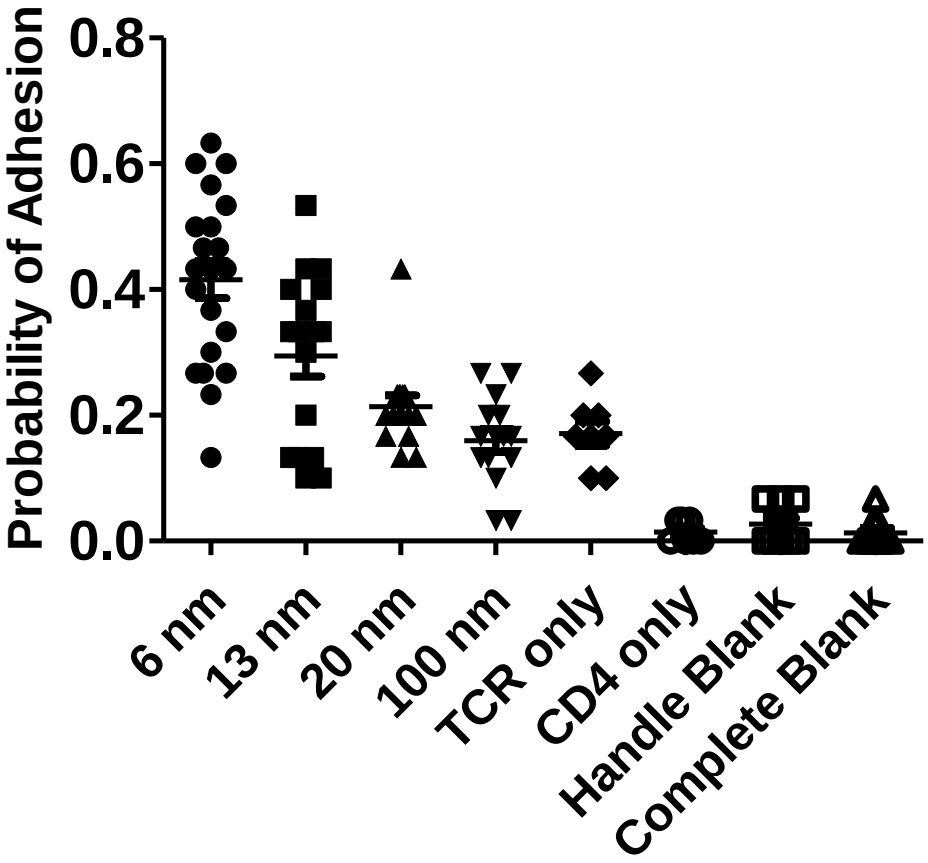

Figure 25 *– Micropipette adhesion frequency results depict probability of adhesion. Each plotted point represents fraction of 30 contacts that exhibited an adhesion.*

(30 times) by piezoelectric-driven micropipettes thus engaging the surface molecules of interest. Deformation of the mechanically ultrasensitive RBC coated with pMHC following a 4-second contact indicated formation of a bond between the opposing surface molecules. The probability of forming bonds was translated into the two-dimensional effective affinity between interacting molecules. When the pMHC coated RBC was brought into contact with beads coated with structures lacking protein handles (HB), or lacking origami (CB), little to no binding events were detected. These frequencies served as a baseline to which molecular interactions of interest were compared to. An indistinguishable number of binding events to those, was observed

between pMHC and CD4, indicating that this bimolecular interaction is not detectable at the molecular site densities used here. However, when RBC coated with only TCR was probed against pMHC at the same site densities, binding was readily detectable at roughly 20% adhesion frequency. Below this frequency, at least 89% of bonds formed were probabilistically interactions between only single TCR and pMHC molecules, as opposed to multimers of either. When TCR and CD4 were multiplexed on the origami 100 nm and 20 nm apart, the degree of binding was indistinguishable from that of interactions between pMHC and TCR only. This result suggests that at these distances, CD4 does not contribute to bond formation between cells. Strikingly in contrast, when TCR and CD4 conjugations were spaced 13 nm apart, bonds formed between cells almost twice as frequently as when they were spaced 100 nm apart ($p < 0.005$). The frequency further increased to more than double what was seen at the furthest distance when TCR and CD4 were spaced 6 nm apart. These results suggest that multiplexing with CD4, whose own affinity to pMHC was not detectable, improves the likelihood that bonds are formed between cells when they are within 13 nm of each other.

To understand the role site densities of each molecule has on the formation of bonds, the probability of adhesion was translated to a normalized surface density of bonds against the number of TCR and pMHC molecules within the contact area. Populations of enhanced normalized bond formation were readily apparent for the 6 nm and 13 nm samples which were distinct from those for the 20 nm, 100 nm, and TCR only samples. These populations were fitted to single gaussian distributions for the 100 nm and 20

nm samples, with R^2 values of 0.8435 and 0.9560, respectively; while a sum of two gaussian distributions were better utilized to fit the data from the 13 nm, and 6 nm samples with R^2 values of 0.9980 and 0.4912, respectively. Therefore, even accounting for site densities, there appears to exist enhanced bond formation when TCR is multiplexed with CD4, despite the lack of detectable bonds between CD4 and pMHC.

Interestingly, there existed distinct populations for both 6 nm and 13 nm samples that did not experience higher number of bonds formation. We speculate that these samples did not present CD4 in the corresponding proximities to TCR due to aberrant origami folding at least in the contact area between cells, which is about 1 μm^2 in area. Together, these results provide evidence for the existence of a critical distance between TCR and CD4 which can improve the likelihood of forming bonds with a pMHC molecule on an opposing cell.

Biomembrane Force Probe Assay

Next, to dissect the quality of bonds formed between the multiplexed origami and pMHC, the BFP force clamp assay was utilized. Here, a glass bead is covalently and densely coupled with streptavidin and attached to the apex of a biotinylated RBC

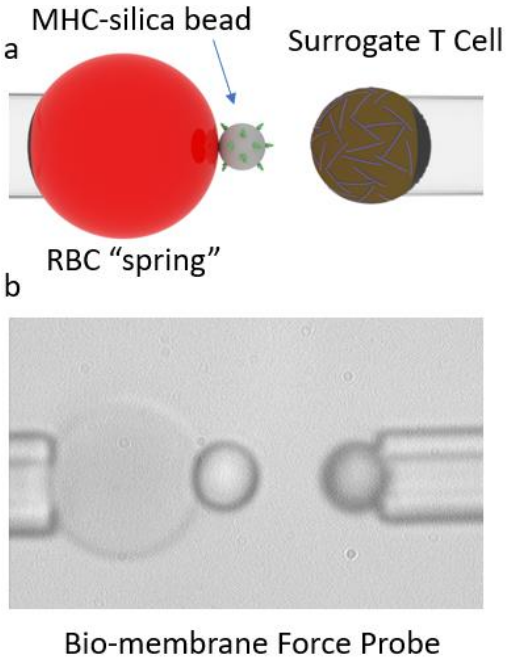

Figure 26 *– Schematic and representative brightfield image of BFP assay.*

whereby the interface between the two is tracked. Bond formation between the origami coated beads and the pMHC coated glass bead will result in displacement of the bead/RBC interface which is translated to force based on a Hookean calibration of the RBC. Bonds were clamped at 15 pN to ensure formation of stable bonds, and each bond event was analyzed further for its stiffness. Extension of the bond that occurred during the ramping phase was calculated by the difference between bead/RBC interface and the distance traveled by the retracted origami bead. A linear regression of the ramp phase data points following 0 pN force represented the stiffness of the molecular bond as the regression preceding it represented the stiffness of the bead. When TCR and CD4 were spaced 20 nm or 100 nm apart, a single gaussian was fitted to the population yielding a mean stiffness of 0.31 pN/nm for both samples. Spacing the molecules 13 nm apart yields the emergence of a stiffer population, and the dataset was fitted to a sum of two gaussians with means of 0.3134 and 0.5781 pN/nm. Lastly,

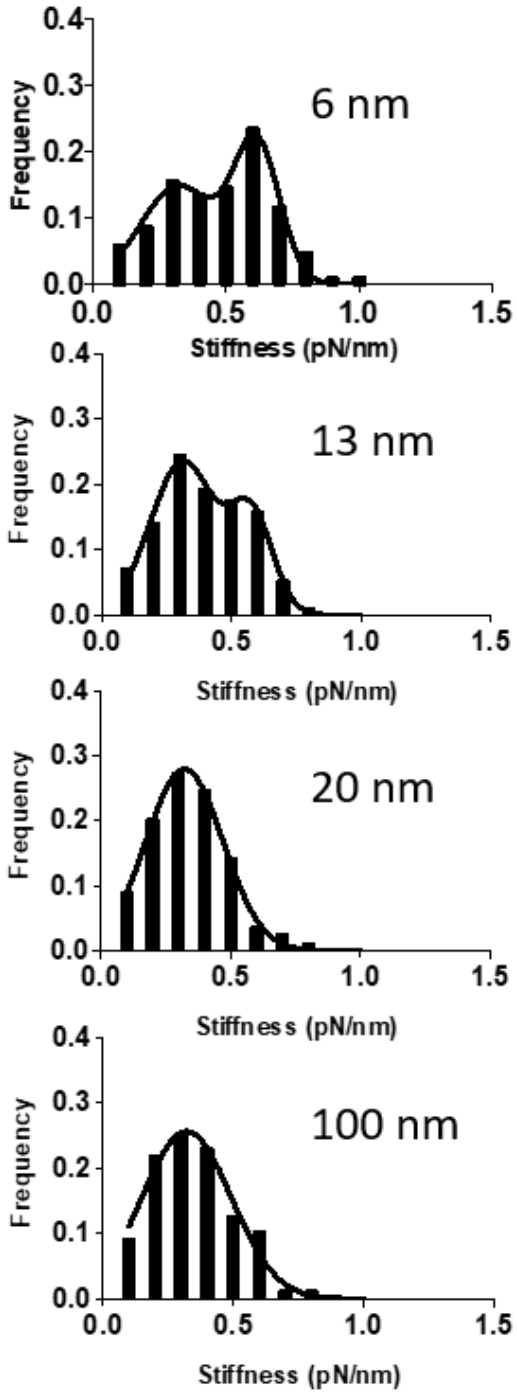

Figure 27 *– Stiffness of bonds formed for various spacings between TCR and CD4*

the 6 nm spacing further promotes the stiffer population of bonds fitted to a sum of two gaussians with means of 0.3195 and 0.6142 pN/nm. These data provided corroboration of the formation of enhanced bonds due to CD4 anchored in close

proximity to TCR. We posit that the stiffer species is a manifestation of a trimolecular bond between the three molecules. The stiffnesses of the 100 nm and 20 nm samples are likely bimolecular interactions, whereby CD4 does not reach MHC, or at least is not of a sufficient distance to allow for the appropriate docking of CD4 to bind to pMHC. It is worth noting that these molecular bonds exist in populations and are in fact reflective of the number of bonds observed using the MAF assay. The 6 nm and 13 nm distances did not guarantee the increased observation of bond formation or stiffer bonds, but instead improved the likelihood that either of those events occur. Future studies should characterize the kinetics of this cooperative bond compared to bimolecular bonds under and in the absence of force. Overall, the data presented here supports the notion that a critical distance exists to promote the formation of trimolecular bonds.

Conclusion

In conclusion, we present the first known case of tuning spacing between two molecules using DNA origami to enable simultaneous binding of those molecules to a third molecule. In using this approach, we reveal the first known direct observation of cooperative trimolecular bond formation and the critical distance at which such cooperativity occurs for this specific set of molecules. Importantly, this is the first demonstration that wild-type human CD4 can contribute to bond stabilization. Future studies will more comprehensively characterize this trimolecular interaction including the respective kinetic measurements as well as discuss its ramifications with regards to T cell signaling. The modularity of the origami conjugation paves the way for facile

investigation of other trimolecular cooperative binding between surface anchored molecules.

Chapter 5: Fluidic Shear Sensor

Many studies have documented how cells biologically respond to hydrodynamic forces induced by flow, through both changes to morphology as well as changes to the signaling pathways. Much research has centered on endothelial cells as they are abundant in larger anatomical features (vessels larger >2 mm), making them easier to study, as well as due to their importance in cardiovascular disease. When shear stress is applied to cultured endothelial cells, they will re-arrange their cytoskeleton to align with the direction of flow in a matter of hours [33]. Decades of research has shown that shear stress alters key signaling pathways including those involved with growth, coagulation, inflammation, extracellular matrix deposition, and more [33]. Such changes have serious implications for human health, as the shear stresses induced from disturbed flow conditions lead to atherosclerosis, a significant source of morbidity. Even in established fields, significant knowledge gaps remain due to a lack of tools. For example, little is known about the role of shear in microcirculation, despite the prevalence of coronary microvasculature disease in millions of individuals [34].

We are just beginning to understand the significance of applied shear stress in numerous other anatomical regions involving a variety of biofluids including urine, bile, milk, blood, lymph, cerebrospinal fluid. Each biofluid interfaces with tissue at a cell-fluidic interface, and all have been difficult to study with existing tools due to their complex geometry and small size. Understanding the influence of shear on these structures is of paramount importance since shear can induce cellular dysfunction that is implicated in the pathophysiology of these cell-tissue interfaces. The key barrier to

further progress has been the lack of direct, easy to use fluorescent reporters that measure the multiaxial and dynamic shear flows that occur *in vivo* across an entire surface of interest, where shear can be directly correlated to physiological changes in cells in real time.

The current paradigm of estimating shear stress at a cell-fluidic interface relies on multiple, complex measurements that are resolved with computational studies and translate poorly to small, intricate geometries. Essentially, a measurement of shear stress depends on a measurement of the change in fluid velocity at the fluidic-cell/vessel interface. Unfortunately, existing approaches such as 4D magnetic resonance imaging (MRI), imaging particle velocities via optical or acoustic techniques (PIV), ultrasound (i.e. Doppler techniques), and surgically inserted probes only measure bulk fluid velocities and lack the precision to gather wall measurements. Instead, researchers couple measurements of the average fluid velocity and vessel geometry to calculate the shear stress at a wall. Measurements of vessel geometry are non-trivial and may involve wax molds of complex shapes. Taken together, this pragmatically means that most studies rely on a significant amount of computational work to calculate wall shear stress from measurements of bulk fluidic velocity and anatomical geometry. Hence, a tool capable of measuring changes in the spatial fluid velocity directly at the vessel wall could greatly simplify this existing paradigm.

In light of this, we envisioned that we could build a nanoreporter that could eventually provide visualization of the shear field applied to the surface of cells, such as the entire

inner lining of a blood vessel, the lumen of pumping lymphatics, within the “harsh environment” bile duct, or numerous *in vitro* systems.

Each bionanomechanical reporter would be similar to a kite (**Error! Reference source not found. 28**) and contains: 1) an antibody-based anchor targeted to a ligand of interest, 2) a DNA or protein-based optical force transducer that fluoresces when unfolded at a threshold force, and 3) a mechanical amplifier (kite) that increases the total force on the transducer. Our data show that a bead (kite) generates tensile force as a function of fluidic drag force and bead size. As the tensile force increases, the optical force reporter, which consists of a series of DNA hairpins with fluorophore-quencher pairs, unfolds and fluoresces.

Extracting Shear from Fluidic Drag Rather than Particle Velocity:

The wall shear stress (τ_{wall}) at a surface is defined as the dynamic viscosity (μ) multiplied by the spatial velocity gradient ($\partial u/\partial y$) at the wall surface, or more formally:

$$\tau_{wall} = \mu \frac{\partial u}{\partial y}\Big|_{y=0} \qquad (1)$$

where u is the velocity, and y is the perpendicular distance from the wall.

Traditional approaches measure the velocity of objects (beads or cells) moving in a fluid and then extract velocity profiles from this data to estimate wall shear. The goal of this project was to create a device that could measure drag near the wall. Moving fluids apply velocity-dependent drag forces to objects, especially stationary or tethered objects, and this principle is responsible for numerous physical phenomena including flying kites, variable rates of sedimentation on different blood cells, as well as drag in automobiles and airplanes. This phenomenon applies to all scales as long as the fluid

may be considered a continuous medium, which pragmatically will apply even to nanoscale structures for liquid water. In the laminar regime, which covers the vast majority of biological structures, drag force is directly proportional to the velocity of the liquid and the size of the object. By measuring the drag on an object of constant size at a specified distance from the wall, we can determine the velocity gradient at the wall. We accomplish this by leveraging the fact that the fluid velocity at the wall is zero (no-slip) and by assuming a linear velocity profile between the wall and object of constant size. Although most flow profiles are not linear, if the distance away from the wall is consistent and minimized (~microns), a linear approximation could possibly be used with minimal error.

Nanoreporter Rationale

DNA mechanotechnology [35] leverages DNA nanomechanics to study biology and provides the unique opportunity to: 1) spatially constrain an object to be within a specified distance of a surface and 2) measure the forces coupled into a DNA strand assembly. We leverage this for the shear nanoreporter by creating DNA nanostructures

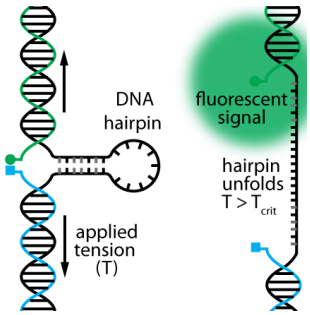

Figure 28 *– DNA hairpins can be designed to unfold at a critical tension leading to fluorescence.*

that constrain the movement of a bead near a wall. The bead's position in relation to the wall depends on lift forces generated near the wall surface as well as drag forces [36]. As the bead experiences drag, which is proportional to the fluid velocity, the DNA strand tethering the bead to the wall experiences tension. This tension is reported optically by ten added hairpins that each have fluorophore-quencher pairs, which fluoresce when unfolded (**Figure 28**). In flow conditions, the system will fluoresce whenever the applied fluidic shear force exceeds a critical value. Changing the number and type of base pairs enables us to create DNA hairpins that unfold at a specified mechanical force.

Given well-defined nano-mechanical and fluidic physics, established DNA-based conjugation techniques, we hypothesized that a DNA bead-based structure could be created to report the wall shear stress applied by a fluid to an interface. We further hypothesized that this structure may be: 1) designed to measure a range of shear stresses; 2) used en masse; and 3) have consistent static and dynamic performance. However, as the physics of polymers behaving near a surface are relatively unexplored due to a lack of tools, we will need to fully characterize the performance of the sensor in numerous constant and dynamic flow situations to test our hypothesis and determine the application space.

Nanoreporter Construction

The fluorescence signal generated from a single fluorophore quencher cannot be detected using confocal microscopy. Previous studies on fluorescent nanostructures show that 10-12 fluorophores contained within the point spread function (~250nm) are

sufficient to create a signal [37]. As such, we designed a nanoreporter featuring 10 serially connected hairpins.

Before we began building the structure, we first selected a sequence to be used for the hairpin force probes in our nanoreporter. The sequence of the hairpin determines the relative force required for the hairpin to opened, as GC base pairing utilizes 3 hydrogen bonds compared to the 2 or AT base pairs. Preliminary calculations suggested the softest published hairpin sequence (22% GC) would be a good place to start, as we planned to test stiffer hairpins after first verifying that the shear flow activated nanoreporter concept was valid [38]. Correspondence with our collaborators in the Salaita lab advised 0% GC hairpins could likely open spontaneously at room temperature, so we began with 22% GC.

With the hairpin sequence selected, we designed a functional unit that could be repeated as desired to increase the number of force-sensing hairpins in series (**Figure 29**). This single functional unit needed five domains, two (one at either end) for connecting to neighboring units and three in the middle for assembling the hairpin and its fluorophore and quencher components. In order to reduce unit-to-unit variability and promote full signal of the serial hairpin assembly in the smallest flow range possible, we conserved the three domains for hairpin-fluorophore-quencher assembly across all hairpin units. Contrarily, the two sticky end domains flanking the hairpin component are unique for all hairpin units. This allows for the rational design of a hairpin chain with a controlled number of units – much like the hierarchical assembly of individual origamis in Chapter 3. At one end of the entire hairpin chain, a digoxigenin modified DNA strand

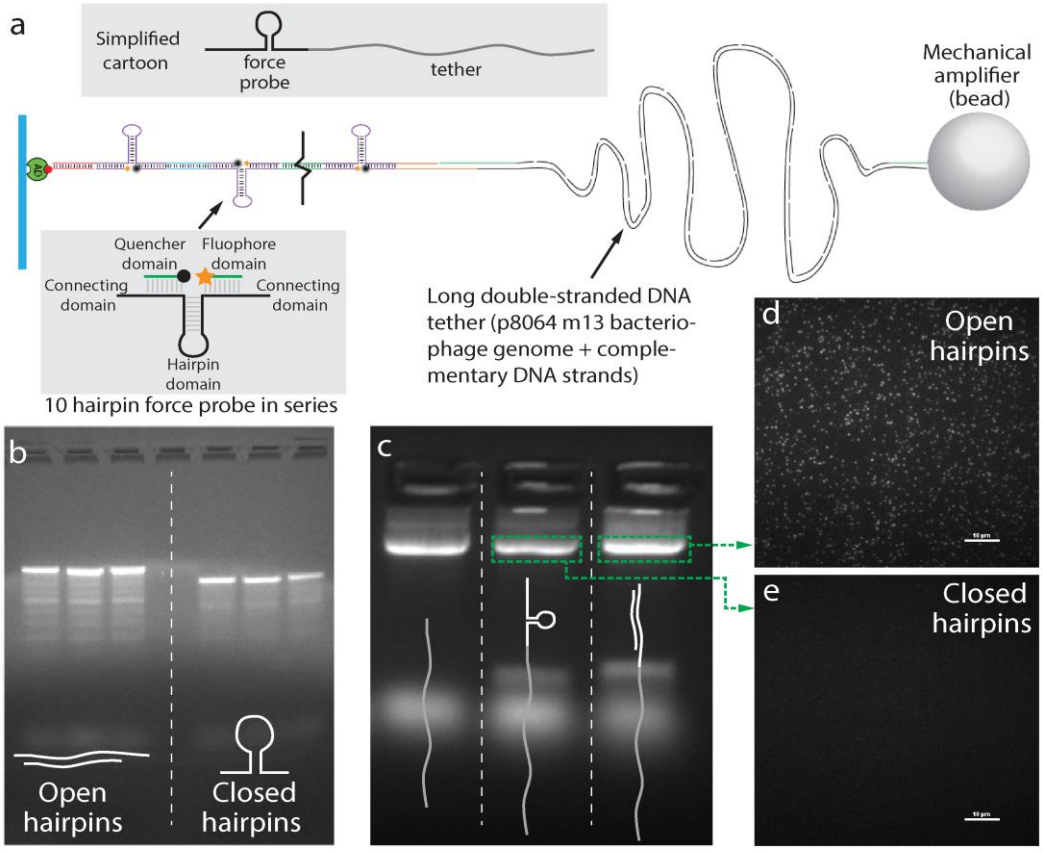

Figure 29 *– We designed (a) & assembled (b-c) a nanoreporter that fluoresces when the hairpins are opened (d; the hairpins were opened by complementary DNA strands and visualized with TIRF) and stay quenched when the hairpins are closed (e). Scale bars are 10 µm.*

is incorporated to allow for selective attachment to a surface bound with anti-digoxigenin protein. At the other end of the chain, a strand connects the hairpin assembly to the long double stranded DNA tether.

The double stranded tether, dsTether, is a modified m13 bacteriophage genome (circular single-stranded DNA, 8064 bases in length) that has been linearized with the restriction enzyme BsaAI at a single location. As p8064 has many restriction sites for the BsaAI enzyme, we had to select for one site to avoid shredding of the tether. To do this, we added a single short oligo to the m13 that made one restriction site double stranded and thus allowed for controlled cleavage at the desired site due to the enzyme necessitating a double-stranded region. Next, after heat-inactivation of the enzyme,

we added a batch of 192 short DNA oligos of equal length to make the long linearized tether double stranded except for a short region on the end opposite the hairpin chain. This single stranded region hybridizes with a connecting strand that captures a biotinylated DNA strand, which binds streptavidin-coated mechanical amplifiers.

To assemble the sensors, we mixed the hairpins, fluorophore, quencher, digoxigenin strand, connecting sandwich strands, unpurified cut m13, 192 short m13 complimentary oligos, and biotin strand together with salted TE buffer. This mixture self-assembles during an overnight annealing protocol in a thermocycler. Finally, the samples are electrophoresed in a 1% agarose gel, and purified by band excision (**Figure 29**c).

Before adding the mechanical transducer component, The efficient fluorescing of opened sensor (by adding complementary DNA strands) and quenching of closed sensor were verified with total internal reflection fluorescence (TIRF) microscopy (**Figure 29** d and e). We added a short oligo complimentary to the entire hairpin to one of the samples, which effectively forces all hairpins in each sensor to adopt the “open” configuration. Samples purified from the gel with this added opening strand exhibited fluorescence while samples without the opening strand could thus adopt the “closed” configuration and fluorescence signal was quenched. It is also worth noting that the linearized double strand tether with added open or closed hairpin chains exhibits gel mobility indistinguishable from the linearized dsTether with no hairpins added. This is because the hairpin chain adds only a few hundred base pairs to the 8064 bp long tether. Additionally, the excess hairpins can be visualized in the gel above the staple

band. However, as the samples are purified based on the mobility of the tether band, visible fluorescence in the open hairpin sample indicates that the hairpins are attaching to the dsTether. We also confirmed that hairpin attachment to the glass depends on the designed digoxigenin/anti-digoxigenin chemistry as very few points of fluorescence were visible in the open sensor sample incubated on glass without prior anti-digoxigenin treatment. In such a scenario, any present fluorescence was deemed to be nonspecific attachment to the glass.

Full Assembly and Testing of Nanoreporter

Following adequate demonstration that the hairpins and tethers were assembling and anchoring to the glass as designed, we attempted to assemble the full nanoreporter with the mechanical amplifier. Addition of the mechanical amplifier would allow for generation of tension in the dsTether and hairpin chain to assess if the hairpins could be opened by addition of shear flow. To test this, we used a simple microfluidic device, consisting of 2mm x 25mm x 100μm PDMS channels attached to a #1.5 coverglass. The microfluidics were incubated with 50 μg/mL anti-digoxigenin for 3 minutes, then washed and blocked with a 1% BSA PBS buffer with Tween-20. We incubated the purified hairpin-tethers for one hour with streptavidin coated silica microbeads washed 3x with 1% BSA PBS buffer + Tween-20. Silica proved to be an optimal bead material due to its low autofluorescence as compared to magnetic or polystyrene beads. Following a 30-minute incubation of the prepared hairpin-tether-bead nanoreporters, the microfluidics were ready for flow and imaging. We hooked up a syringe pump with

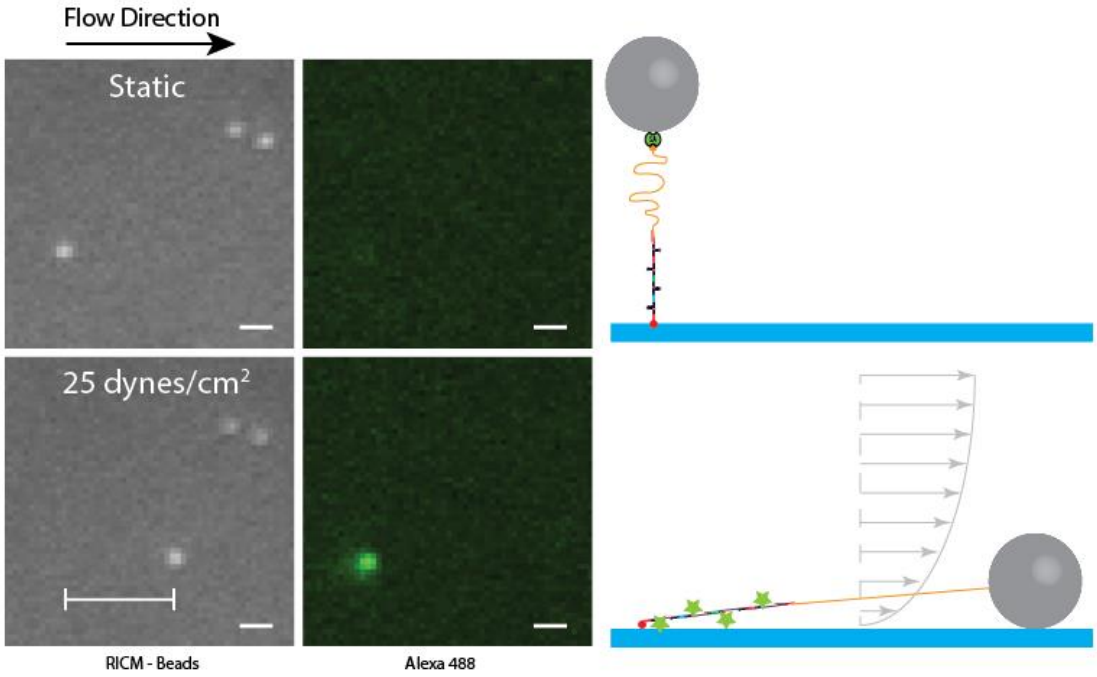

Figure 30 *– When flow is applied within the microfluidic, the active nanoreporter bead is pulled downstream by drag forces which opens the hairpins and allows fluorescence. Inactive, nonspecifically bound beads do not move under applied shear. Here, the shear stress is approximately 25 dynes/cm^2 (2.5 Pa) for a 1 µm bead. Scale bars 1 µm.*

PBS and connected the microfluidic with friction fit tubing. By applying gradually increasing shear, we found that the hairpins began opening at 15 dynes/cm2 and gradually increased in fluorescence intensity until about 25 dynes/cm^2 was applied for a bead size of 1 micron in diameter (**Figure 30**). Further increase in applied shear did not result in increased fluorescence, indicating that all 10 hairpins were opened in equilibrium. Following removal of shear, fluorescence signal likewise promptly disappeared. We confirmed that this process could be repeated many tens of times, or until the fluorophores bleached.

Furthermore, when viewed with brightfield or RICM imaging, the beads can be seen moving around via Brownian motion in a zero shear environment. Upon application of shear flow, the beads move in direction of the applied shear then stop after having

displaced around 2.7 microns, which is the length of the tether. Since the beads are not stationary when no shear is applied, measuring the exact displacement is difficult. Anyway this controlled displacement indicates that the beads are tethered to the surface, and is helpful for identifying active nanoreporters as beads nonspecifically bound to the glass do not move when shear is applied.

Another important point pertaining to the ability of these nanoreporters to directly measure shear is the bead's exact vertical location. Given that the flow velocity profile near the wall may be linear, a bead anywhere within this linear region would technically experience the same shear. However, within this region, a bead further away from the wall will experience greater flow velocities and thus generate more drag. As such, function of the nanoreporter is inexorably tied to flow velocity, and thus the bead's vertical position within the flow profile. For the nanoreporter to be called a shear sensor, and not a flow sensor, its bead must be in approximately the same y position in all sample and testing conditions. During our preliminary experiments, this is exactly what we observe. Tethered beads move freely in static conditions, and often are barely visible in RICM imaging as they float around over a micron away from the glass. But in flow conditions, even just a few dynes/cm^2, the beads will come down to the glass. This tells us that the nanoreporter beads are sensing flow velocity conditions consistently with the mechanical amplifier in the same y location, which is right up against the glass. Given this, we feel comfortable designating our nanoreporter as a shear sensor. However, we also recognize that this means that mechanical amplifiers of different sizes cannot be directly compared, as different sized beads experience

different ranges of the flow profile even up against the glass.

Even with all the consideration about how the nanoreporter can be considered a sensor of shear, we conducted some preliminary experiments with different size beads. Knowing that drag force is proportional to cross-sectional area, we expected a bead size of 0.5 microns in diameter to require about four times the shear for hairpin activation. We witnessed this experimentally and also confirmed that a 5 micron bead requires significantly less shear for hairpin activation, which was consistent with our estimates.

Improved Nanoreporter Yield

Our first experiments revealed consistent and repeatable nanoreporter function, but with few sensors per unit area compared to how many beads were being added to the chamber. Taking a pointer from the previous chapter where we discovered origami loading onto beads required an overnight incubation, we first investigated if the yield of active sensors on glass surface could be dependent on the duration of the hairpin-tether with microbead incubation. We found that instead of 1 hour, an overnight

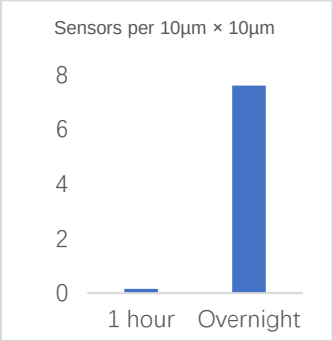

Figure 31 *– Preliminary optimization improves active sensors per unit area.*

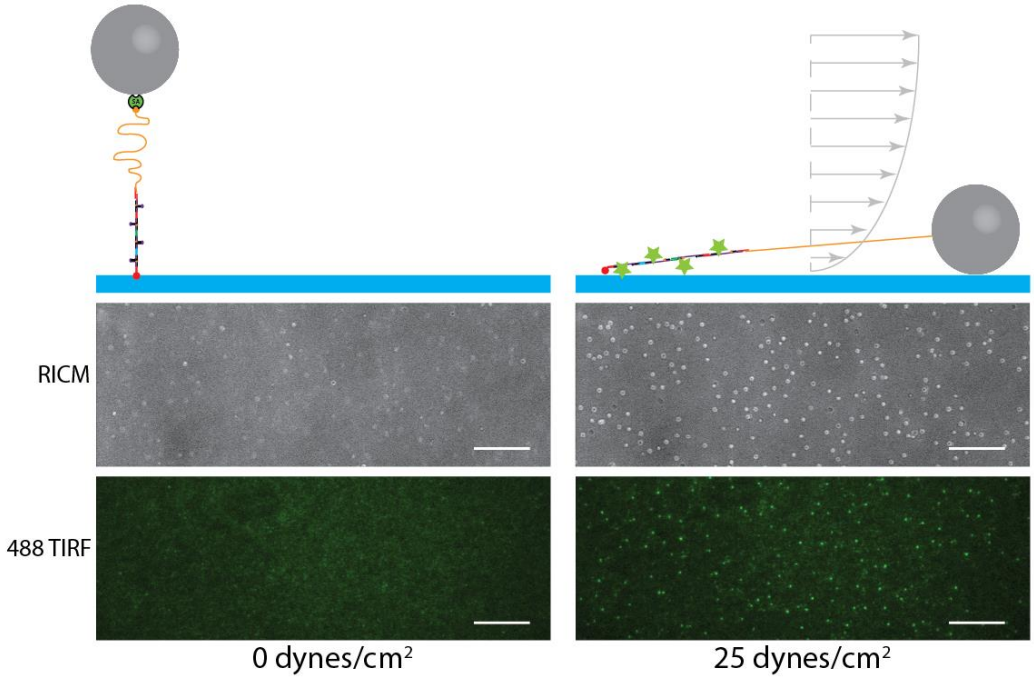

Figure 32– *When flow is applied within the microfluidic, the bead is pulled downstream by drag forces which opens the hairpins and allows fluorescence. Here, the shear stress is approximately 25 dynes/cm^2 (2.5 Pa) for a 1 µm bead. We can easily tailor the threshold shear by changing the bead size or hairpin sequence. Scale bars 10 µm.*

incubation on a rotator increased active sensors per unit area over 50-fold (**Figure 31**). Additionally, blocking both the glass surface and the beads with a PBS + Tween-20 + 1% BSA solution is also necessary. Otherwise, the entire glass surface would be covered with nonspecifically bound beads. We also discovered that large nonspecifically bound clumps of beads could be removed by a brief sonication of the beads after washing and before incubation with the dsTethers. Other areas of optimization that can be investigated in the future are anti-digoxigenin concentration on glass, bead-tether-hairpin incubation on glass, and different blocking buffers.

Multi-valent Mono-active Tether Attachment

As the protocols used to create the nanoreporters would logically result in beads with more than one dsTether/hairpin chain attached to it (10x excess molar incubation of

dsTether onto bead), we hypothesized the beads might be multivalent yet mono-active sensors. This means in a given flow direction, only one of the bead's multiple tethers would experience tension and therefore produce fluorescent signal. We confirmed this by subjecting the same region of interest with different directions of flow. Some of the fluorescing hairpin chains remained in the same location regardless of which direction of flow – thus suggesting the specific nanoreporter was truly monovalent. Other beads displayed disappearance of one hairpin chain but the appearance of another one upstream of the new flow direction relative to the first hairpin chain signal. Furthermore, reverting the flow direction results in a return of the initial hairpin chain location.

Multi-valent Multi-active Tether Attachment

While holding bead concentration and incubation times constant, the number of tethered beads on the glass surface is proportional to the concentration of purified hairpin-tethers incubated with the beads. We found that as the tether concentration is increased to about 200 pM, the active 1-micron diameter beads per 100 square microns peaks at ~8. Further increase of tether concentration instead produces a

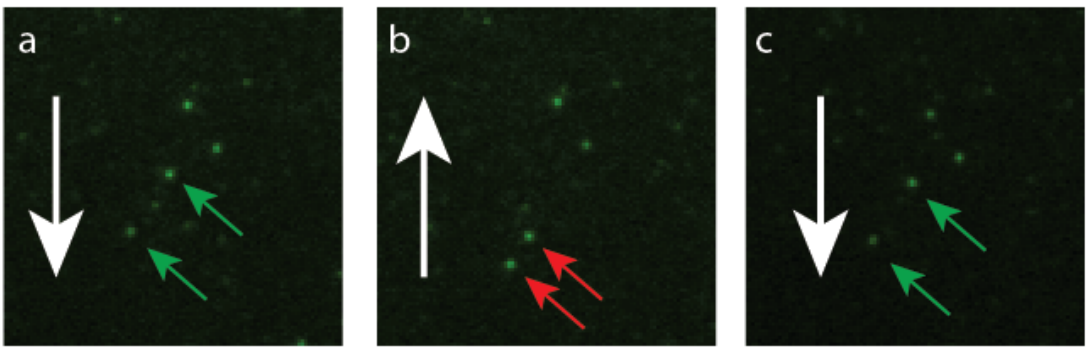

Figure 33 *– Four fluorescent nanoreporters are visible (a). Upon reversal of the flow direction, the bottom two nanoreporter signals appear in different locations upstream of the flow direction (b). After restoration of the original flow direction, the original two nanoreporter signals reappear (c).*

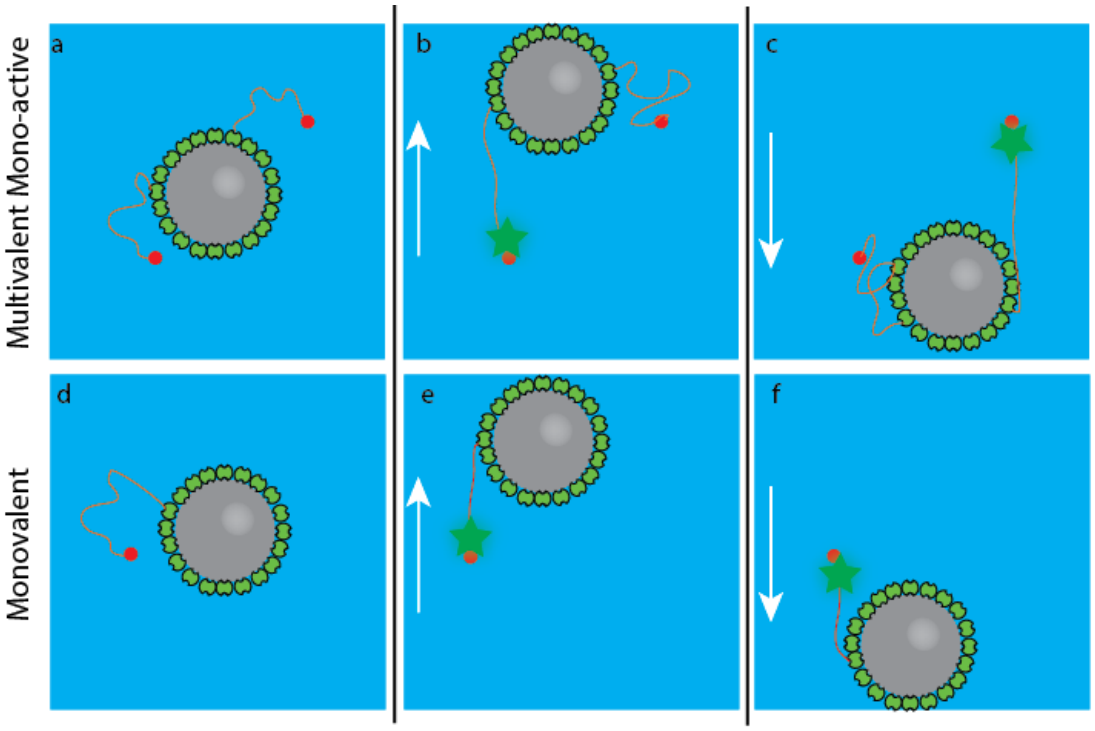

Figure 34 *– Illustration of multivalent monoactive (a, b, c) and monovalent monoactive (d, e, f) concept. Multivalent nanoreporters can still be monoactive if the hairpin chains are spaced far enough apart (b, c). Changing flow direction changes which hairpin chain experiences tension (b, c). Monovalent nanoreporters demonstrate a single fluorescence location no matter what direction the flow is applied (e, f).*

proportional increasing prevalence of a second population of beads that are connected to more than one active hairpin-tether. The phenotype of this multi-active nanoreporter is two or more fluorescent spots near each other which are relatively perpendicular to the direction of flow, and visibly associated with a single bead. We also observed an increased flow rate is necessary to elicit full hairpin opening in the multi-tethered nanoreporter – suggesting that the drag force is being shared in parallel across the two hairpin chains. At 200 pM dsTether, the occurrence of this multi-active nanoreporter is less than 1%, but at 500 pM dsTether, beads with 3 or even 4 active hairpin chains are commonplace. We envision special cases like this offer unique opportunities to study and reinforce understanding of shear stress, velocity, force, and

DNA biomechanics models at the nanoscale, and plan to study them in the future.

Out of curiosity, we tried to take the concept of multivalency to the extreme by using a very high tether concentration of 1.4 nanomolar. In order to produce a tether concentration this high, the hairpin chain and tether assembly processes were separated. The surface was saturated with 15 nM of purified hairpin chains, while the beads were incubated with varying concentrations of double stranded linearized m13. In **Figure 35**, the high concentration of dsTether resulted in beads with highly restricted movement. Even in static conditions, the beads appeared to be tied down to the glass, demonstrating less than half of the usual displacement under flow. We describe this scenario as “Supervalent” and provided an artistic rendition in **Figure 35a**.

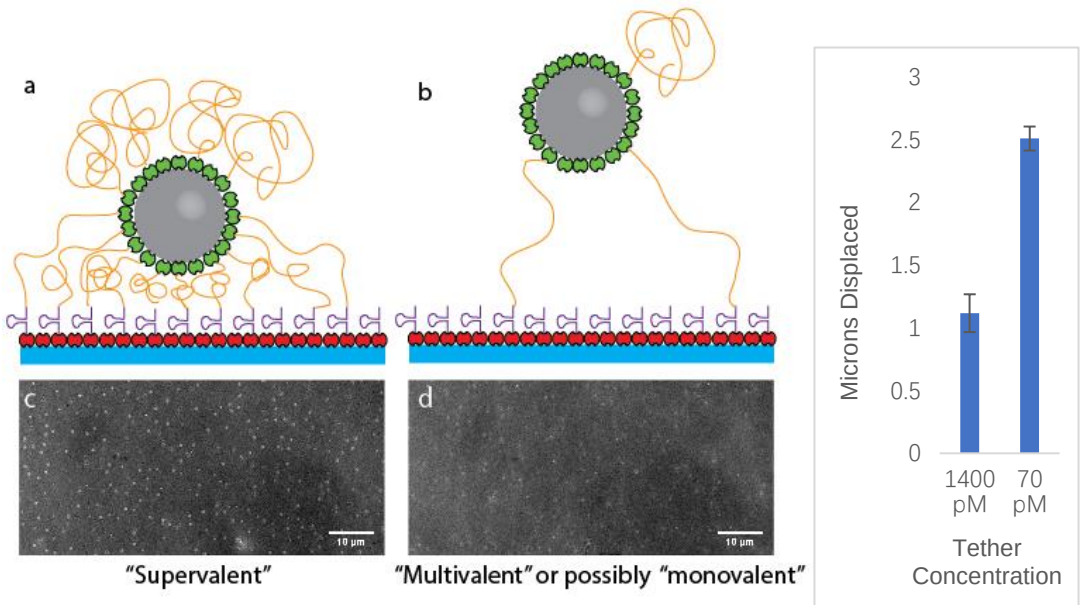

Figure 34 *– High concentration of dsTether DNA results in a ‘Supervalent’ bead that has heavily restricted movement. RICM imaging shows beads bound close to glass in static conditions. Lower valency allows for beads with mobility which float above the glass and are not easily visible with RICM. With applied shear, supervalent beads demonstrate restricted movement with only 1 micron displacement, compared to the 2.5 microns of low valency beads. Scale bars 10 µM*

Future Work – Expanded nanoreporter functionality

Our work so far has demonstrated a novel molecular shear sensitive nanoreporter consisting of a microbead, DNA tether, and fluorescence force transducer. To fully explore the design space of this approach, we will synthesize a library of nanoreporters with different features, and systematically verify their yields and performance by using the aforementioned methods. We specifically will modify: 1) the DNA hairpin sequence, which determines the threshold force for the opening of the hairpin; 2) the number of hairpins in the fluorescence force transducer; 3) the size and material of the microbead, and 4) the length of the DNA tether. Each one of these design parameters will affect the behaviors of the nanoreporter. By studying a library with different combinations of these design parameters, we expect to develop a family of robust, sensitive, tunable nanoreporters that accurately respond to a wide range of shear forces. We will perform this task by assembling purchased DNA hairpins of different sequences and microbeads of different sizes. The DNA tether will be prepared by using m13 DNA. Longer DNA tethers can be produced by using lambda DNA, or by hierarchically assembling multiple m13 DNA strands. Shorter tethers can be prepared by cutting the current m13 scaffolds into approximate desired lengths with restriction enzymes.

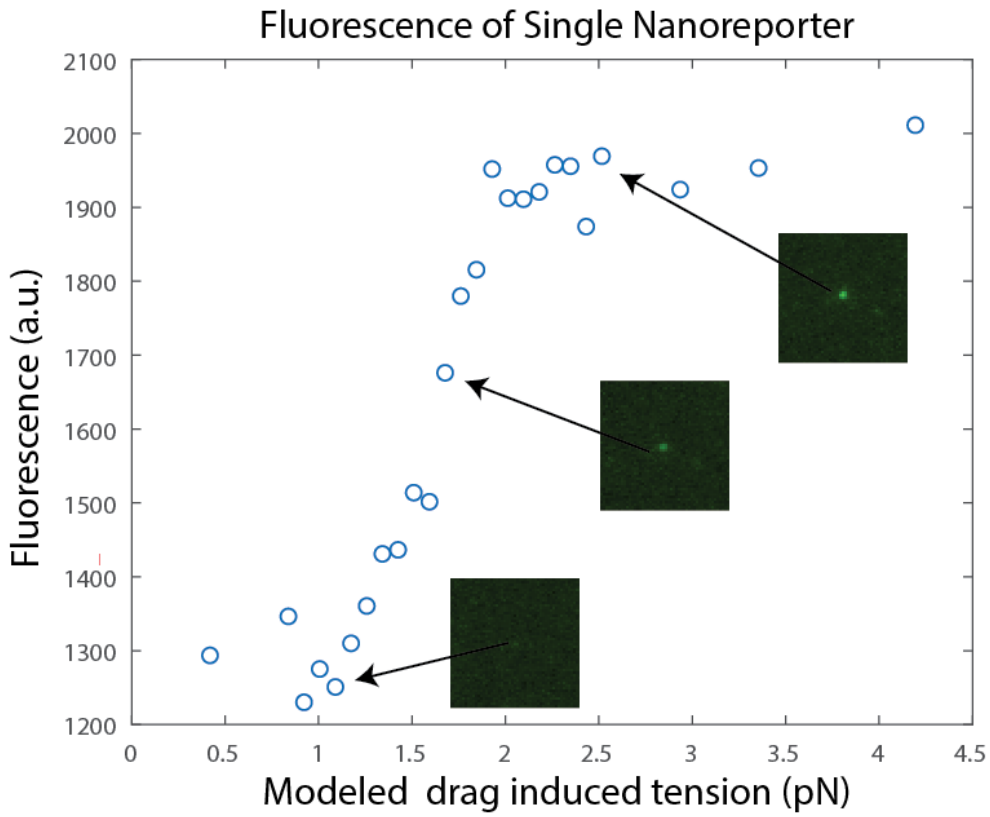

Figure 36 *– Sigmoid curve of fluorescence intensity from a single hairpin chain in response to increasing applied shear. X-axis tension values are preliminary results of modeling efforts.*

Future work – 22% GC Hairpin $F_{1/2}$ modeling

Our data show that the hairpin chain opens over a narrow range of applied shear stress. After a base flow rate is reached, the fluorescent signal increases with flow rate until a maximum where all hairpins in the sensor assembly are open. Quantification of this fluorescence yields a sigmoid curve of the hairpin assembly's active range (**Figure 36**). This means that at a given flow rate within the range of this sigmoid curve, an equilibrium number of hairpins in the 10 hairpin chain are open. Our collaborators in the Salaita Lab recognized this could be an excellent opportunity to use the flow rate where 50% of hairpins are open to back calculate the force required to open 50% of the hairpins, or the $F_{1/2}$.

$$F_d = \frac{1}{2} C_d \rho A v^2 \qquad (2)$$

Preliminary modeling results reveal an $F_{1/2}$ of 1.5 pN, which is within the ballpark – but significantly different than – the expected 4.7 pN for the 22% GC hairpin. We quickly came to realize that modeling is more difficult and complicated than we originally thought, as equations for fluid velocity at specific microfluidic heights do not directly translate to microbeads with finite size spanning a range of gradually changing flow velocities. As we continue research and expand our experience and knowledge of the system, such as how much the dsTether itself contributes to drag, we will strive to improve the accuracy of our models for the applied drag force. In addition, we plan on repeating this quantification process with different bead sizes, channel dimensions, and in varying channel locations to calibrate and cross verify our models.

Bead velocity measurement

In preparation for our studies in modeling the nanoreporters force response behavior, we attempted to experimentally measure the velocity of the beads during flow, as knowing bead velocity is necessary for calculating the drag they produce. Recognizing

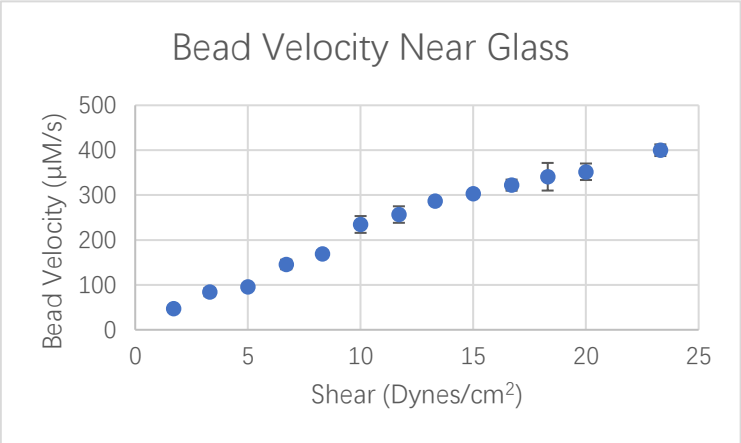

Figure 37 *– Experimental velocity measurements of near-glass bead velocity by measuring length of bead streaks per frame during RICM imaging. N = 5*

that flow velocities vary drastically with height in the microfluidic, we used RICM instead of brightfield to visualize beads specifically at the glass surface interface. We took videos of free untethered beads at gradually increasing flow rates, and measured visible streaks in a single frame. These streaks represent the distance the bead travelled during the frame, which had a known duration of 21 milliseconds. Plotting our data, we discovered a mostly linear velocity increase in response to flow rate. This data will be used to corroborate calculations based on derivations of the Navier Stokes equation for fluid velocity at a specified height in a rectangular cross section fluidic channel.

Future Work – Rheometry Validation and Feature-Bearing Microfluidics

To apply shear stress, cone and plate rheometry represents the gold standard approach to applying a precise, uniform shear stress. Rheometers induce Couette flow by suspending a liquid between a bottom stationary flat plate and moving top conical-shaped plate. In Coutte flow, the velocity will linearly increase from zero at the stationary plate to the velocity of the moving plate. The velocity in the liquid (and applied shear stress) is directly linked to the velocity of the top plate, which is easy to both control and measure with high precision. Since the motion of the plates is rotational, and due to the introduction of the cone, the shear stress experienced anywhere on the plate is constant.

We will purchase a TA Discovery rheometer with fixtures for imaging fluorescent objects in Coutte flow. This system is functionally similar to an Anton Parr rheometer that we have used previously [39]. Based on our current results, we anticipate being

able to use a 63x objective (NA 1.3) to image and quantify the fluorescence of single nanoreporters. Here, we will validate our nanoreporters with bead sizes ranging from 0.5 μm to 5 μm in diameter. We will test the optical fluorescence and determine the fluorescence intensity, for each, testing over shear stresses from 1 to 10,000 dynes/cm^2. We will extract the $F_{1/2}$ for each sensor as well as the maximum shear that can be sustained before failure. We will then test the dynamic response of the sensor by increasing the frequency of oscillation from 0.5Hz to 10Hz, as these range will cover typical frequencies (heart beats) that would be expected *in vivo* for humans and murine animal models. Pass criteria include consistent performance in all tested sensors (less than 10% variance) and an accurate measurement of shear in over 90% of sensors.

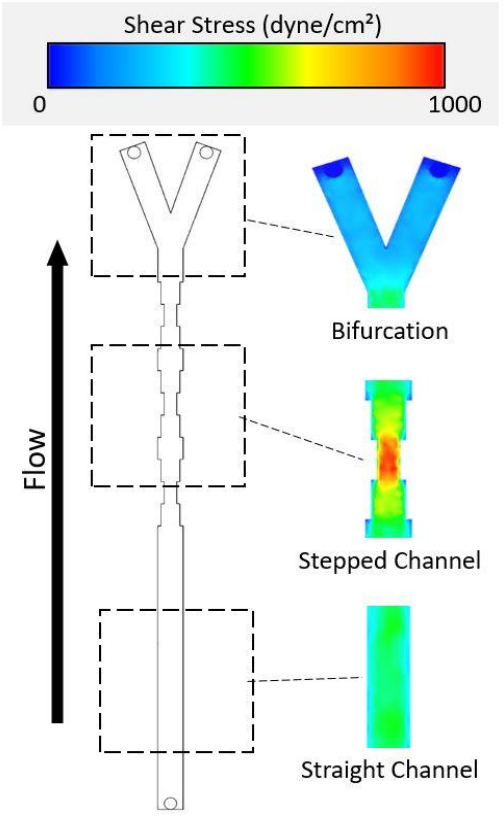

Figure 38 *– We have designed a microfluidic with multiple test structures that have spatially varied wall shear stress to characterize the nanoreporter performance*

Microfluidic devices offer the opportunity to precisely control the geometry of a fluidic structure as well as the applied flow rates. In addition, spatially complex shear stresses can be created over small volumes that can be imaged using standard confocal microscopy. To that end, we have designed a microfluidic with a complex spatial shear stress that can be used to test the spatial response of the nanoreporter (**Figure 38**). The microfluidic features a straight channel with uniform shear, a bifurcation, and stepped channels to create shear that varies by an order of magnitude. We will create the structure using standard soft-lithography methods that we have significant amounts of experience designing and fabricating [39-43]. Briefly, molds will be created on

100mm silicon wafers with SU-8 photoresist and heights will be carefully checked using a Dektak 150 profilometer to ensure a consistent height. Based on results from our previous experiments, we will examine the accuracy of nanoreporters attached to a microfluidic with varying shear forces and gradients. Again, pass criteria will be consistent performance (<10% var) and >90% accuracy.

Future Work: Scaffolded Nanoreporter

One of the major concerns of the current design which utilizes serially connected hairpins is that there are many individual pieces linked together, where failure in any one of said components would result in failure in the entire nanoreporter. This also limits the number of hairpin chains that can be used, as adding more hairpins for brighter signal would further reduce yields and complicate assembly. As such, we are designing a scaffolded version where all force sensitive components are included on the long linearized tether strand. This way, all tension is bore on the continuous tether, and not across unligated sticky ends. Our preliminary exploration into this design appears to suggest non-specific interactions between the scaffold loops. We plan to add short staples into the loop to reduce secondary structure in such a way that does

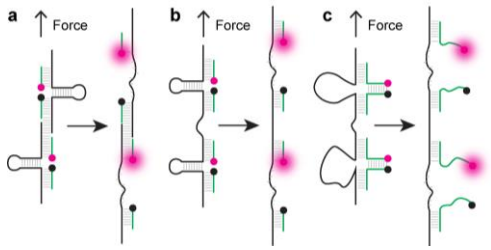

Figure 39 *– Alternative DNA force transducer designs. (a) The designed used in preliminary study. (b) and (c) Alternative designs that utilizes the long tether as a backbone.*

not add tension to the hybridization between fluorophore and quencher strands.

Construction of Bio-Inspired Shear Nanoreporter

Von Willebrand Factor, an ultra large concatemeric blood protein, nominally circulates in a coiled compact form. Upon injury, VWF attaches to exposed collagen, unfolds, and facilitates platelet binding via a force sensitive binding site (high affinity in high shear) [44]. Inspired by von Willebrand Factor (VWF), we hypothesized that a shear nanoreporter could also be created using only DNA-based organic components (i.e. no bead). Building on our bead-based idea, we sought to create a shear nanoreporter that utilizes an organic structure to generate drag forces. Although less intuitive, drag is induced on linear structures, and the total applied force is proportional to the square root of the length of the polymer, i.e. extension $\propto L^{1/2}$ [45]. This suggests that polymers of sufficient length can be used to measure the applied shear stress if a reporter is incorporated into the structure. We decided to investigate this approach as it has a few significant advantages as compared to bead based approaches. First, a completely biomolecule-based structure is more biodegradable and would have improved *in vivo* compatibility. Second, the simplified chemistry (the assembly of nanoreporters mostly driven by DNA hybridization) streamlines the assembly process and potentially improves the yield and stability of the nanoreporter. If non-specific adhesion is encountered, the simplified chemistry should also make troubleshooting easier. Finally, it provides additional flexibility on designing nanoreporters with different geometries (e.g. dendrimers), which enables detailed study on the shape effect and allows us to custom-design nanoreporters adapted to constricted anatomical locations.

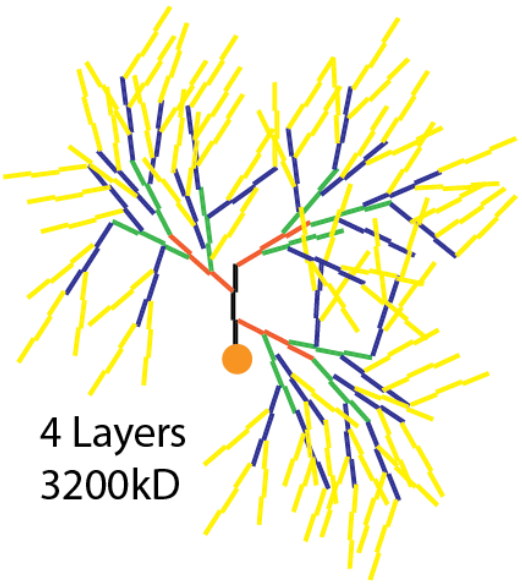

Figure 40 *– 3.2 megadalton dendrimer composed of five unique DNA strands. Each subsequent layer has three times as many components as the last. Can be modified to be fluorescent with Alexa 647*

Dendrimer Structures Generate Drag in Flow Conditions

To replace the bead mechanical amplifier, we needed a structure that could continuously be scaled up, occupy a three-dimensional space with high surface area, and be simple in design. To satisfy these needs, we chose a DNA dendrimer-type construct where each layer consists of 3X more DNA strands than the previous layer. By first employing a single fluorescent dendrimer in place of the bead, we verified that the tether/hairpin assembly was extending as a result of applied flow. An interesting side effect of attaching the fluorescent dendrimer to the dsTether was that they became easily distinguishable from dendrimers nonspecifically attached the glass. The active dendrimers appeared in the exposure as a fuzzy cloud of fluorescence, as they experience Brownian motion but are ultimately constrained by the dsTether. Contrarily,

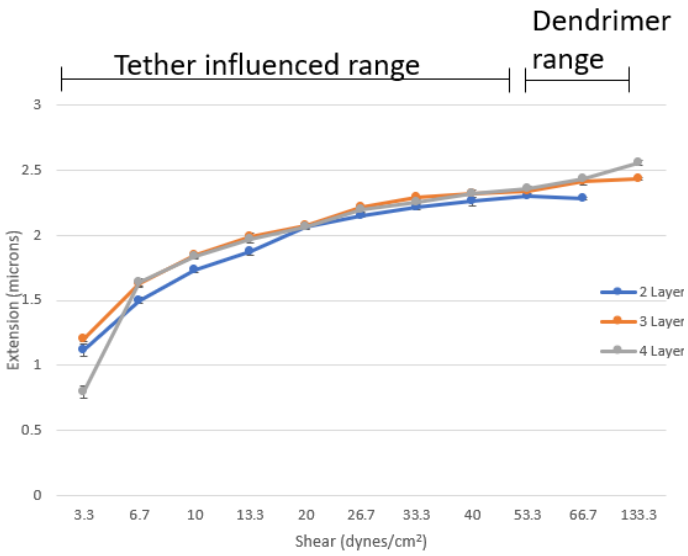

Figure 41 *– Extension of dsTethers with different size end dendrimers as a function of applied shear. Dendrimer size appears to contribute little to tether extension until over 50 dynes/cm^2. N=5 for each point.*

nonspecifically attached dendrimers appear as sharp points of fluorescence as they are stationary. In **Figure 42**, in static conditions, the fluorescent dendrimer can be seen co-localized on top of constitutively open hairpins. After application of shear, the dendrimer fluorescence displaces from the hairpin chain fluorescence in the direction of flow. With increasing applied shear, the displacement of the dendrimer from the hairpin chain increases. We confirmed that the dsTether could be stretched further, and that displacement of the dendrimer from the hairpins did not exceed 2.8 microns, which is the designed length of the dsTether.

Next we repeated the experiment with closed hairpins and attempted to increase the size of the dendrimer so it could generate enough drag to open the hairpins. Using the largest dendrimer we had at the time, 4L dendrimer with 3.2 MD mass, we failed to see any hairpin signal even with shear increased to almost 300 dynes/cm^2 – approaching the limit of our friction fitted microfluidic system.

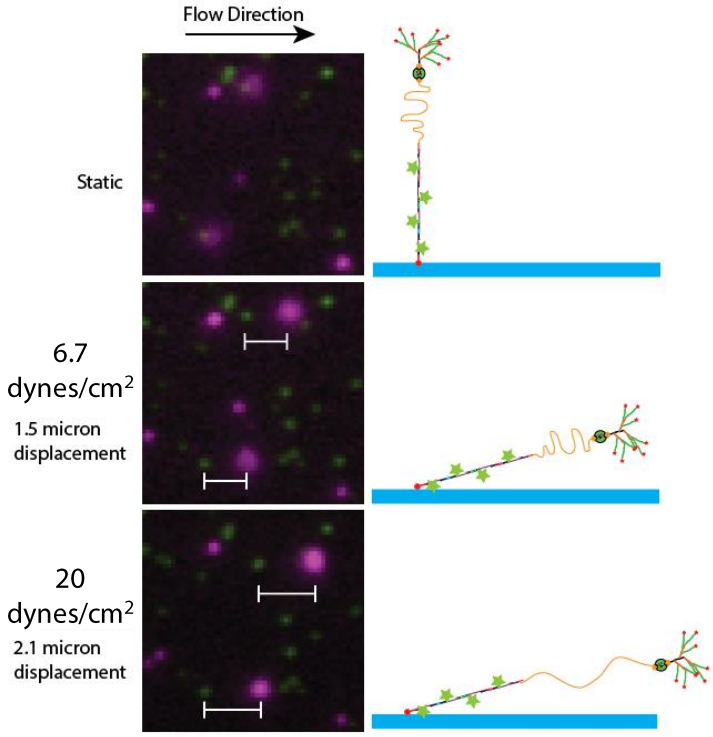

Figure 42 *– dsTethers with end conjugated fluorescent dendrimers extend under shear. Here, we fluorescently tagged a dendrimer structure and tracked its motion relative to constitutively open hairpins. In flow, the total distance from the dendrimer (end of nanoreporter) to the hairpins (base of nanoreporter) varies with flow as expected.*

To better understand how the dendrimer/tether system responds to shear, we repeated the open hairpin experiment with three different dendrimers: 2L (300 kD), 3L (1 MD), and 4L (3.2 MD). At a spread of different applied shears, we found that the measured amount of tether extension was almost the exact same for all three dendrimer sizes. The only noticeable difference was at very high shear rates for the microfluidic, where the larger dendrimers produced greater extension than the smallest one. This suggested to us that the dendrimers were barely contributing to the dsTethers extension, and that the long double stranded DNA could indeed extend in flow by itself. We later confirmed this by removing the dendrimer entirely and modifying the tether

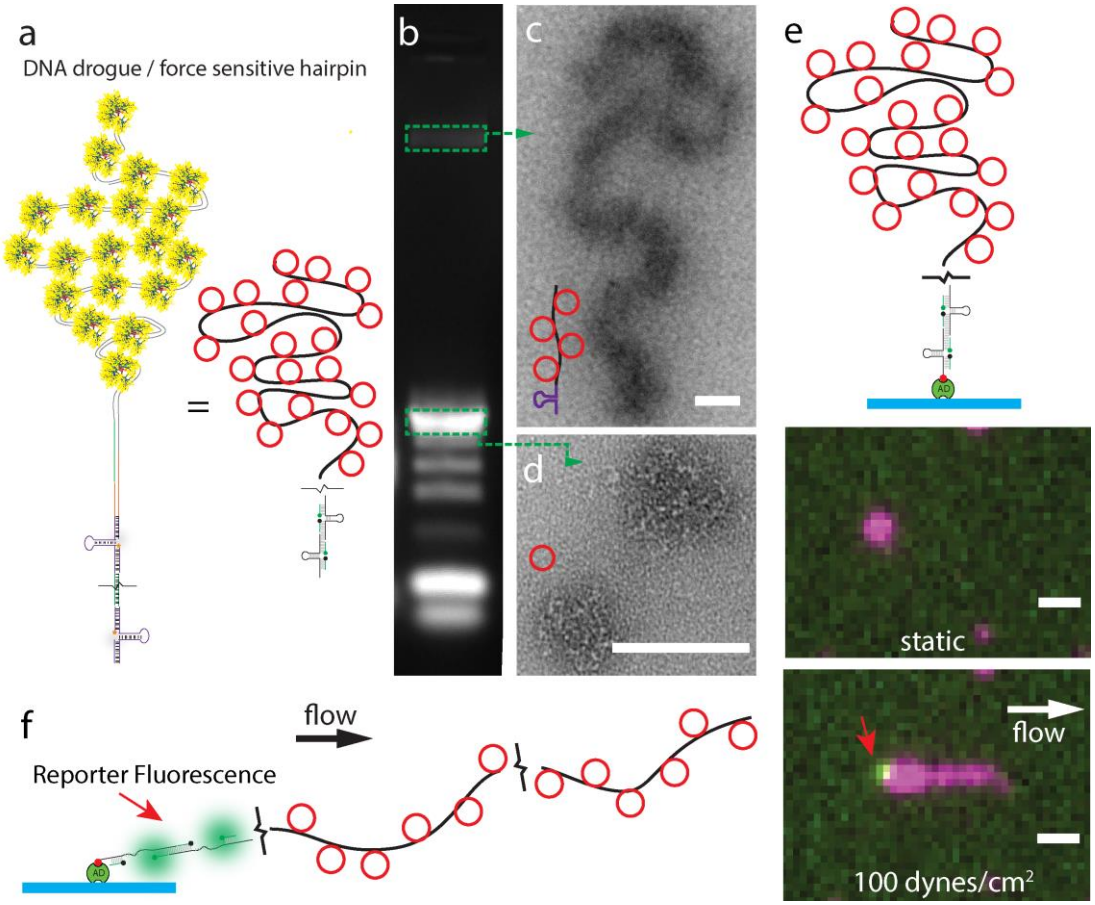

Figure 43 *– 192 5-layer (5L) Dendrimers added to the dsTether to create shear reporting DNA drogues (a). Following agarose gel purification (b), hairpin-DNA drogue (c) and four-layer dendrimer TEM images (d), scale bars: 100 nm (c, d). DNA based shear sensor with un-optimized DNA drogue mechanical amplifier can detect high shear stresses (100 dynes/cm^2) (f). Scale bars: 1 μm (e, f).*

itself to be fluorescent.

DNA Drogues Generate Sufficient Drag Forces to Open Hairpins in High Shear Conditions

While we confirmed that the dendrimer enabled extension of the tether in flow, a single dendrimer was not generating enough force to open the hairpins. Inspired by storm drogues, which are long underwater parachutes that trail behind and stabilize boats by inducing drag in stormy weather, we used many dendrimers to create a DNA drogue. Specifically, we added as many dendrimers as possible (192) onto the tether by incorporating a dendrimer capturing extension on every short oligo used to make the

linearized p8064 m13 double stranded. These capturing extensions hybridize the backbone strand of each dendrimer, or the strand that every other strand branches off of. This way we could program a controlled number of dendrimers to hybridize to the long tether. We compared DNA drogues comprised of 3L, 4L, and 5L dendrimers respectively. During flow testing, only the 5L dendrimer managed to produce fluorescent signal.

The 5L dendrimer DNA drogue has a total designed mass of 2.2 billion Daltons. Although this is an incredibly large DNA structure, it still runs into the agarose gel with limited aggregation in the wells. We observed that this DNA drogue shear nanoreporter could produce signal at high shear rates of 100 dynes/cm2 (**Figure 43**e). TEM imaging after agarose gel purification revealed a long and snakelike electron-dense megastructure. Notably, the DNA-based mechanical amplifier generates less drag than the bead-based design, and can likely be improved further with additional studies into better DNA-drogues.

Future Work: Giant DNA Drogues

With the verification that it is possible to open hairpins with drag generated from DNA alone, we will engineer even larger DNA drogues. We will explore two possible strategies to accomplish this: (1) adding more layers per dendrimer or (2) using multiple long DNA drogues with a single hairpin chain. As it is easier to add more layers, we will pursue this option first simply by designing, ordering, and adding subsequent layers to the dendrimer. We may, in the interest of reducing steric hindrance, switch from 1:3 layer n-1 to layer n ratio to 1:2 or 1:1 in the planned additional layers. Importantly, data gathered from adding more layers will be used to inform models of drag forces on the dendrimer and guide our next steps. A key goal of this work will be to generate new scientific data for the broader community on the biophysics of complex oligonucleotide structures in flow conditions. The second option will be to use multiple long scaffold DNA to create an even larger structure, specifically using an intermediate

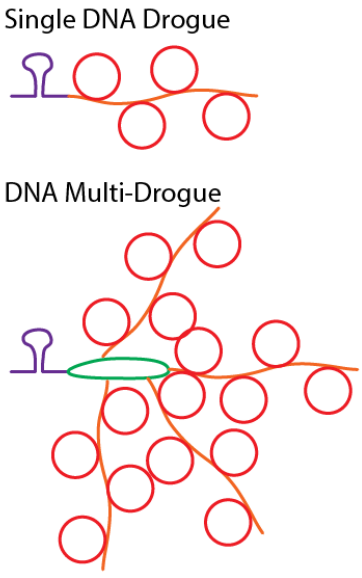

Figure 44 *– Planned method to multivalently attach several drag generating DNA drogues onto a single hairpin chain.*

size circular p3015 m13 DNA to simultaneously grab many fully formed DNA drogues. We will start with just a few DNA drogues and assess their influence on shear stress detection threshold. Our goal is to create a structure capable of extending the possible working range of DNA-based shear nanoreporters from 100 dynes/cm^2 to 10 dynes/cm^2.

Targeting of Shear Nanoreporter to Cells

As mentioned previously, shear may affect numerous cell types in various anatomical locations. A key aspect of measuring the shear stress on these cells will be attaching a nanoreporter directly to the cell surface. This can be accomplished by conjugating molecules or proteins to the nanoreporter that will facilitate cell binding. Targeting specific antigens on the cell surface confers the additional advantage of targeting specific cell types and even cellular states. For example, vascular cell adhesion molecule-1 (VCAM-1) is expressed on activated endothelial cells [46] and a key marker of pro-atherosclerotic conditions. Hence, a shear nanoreporter targeting VCAM-1 will identify when pro-atherosclerotic conditions are present and report on the localized shear in that area. Importantly, given the versatility of DNA, numerous biomolecular conjugation techniques are available to bind targeting molecules to DNA. As such, we hypothesize that a properly conjugated shear nanoreporter can be created such that it binds to a specific cell type.

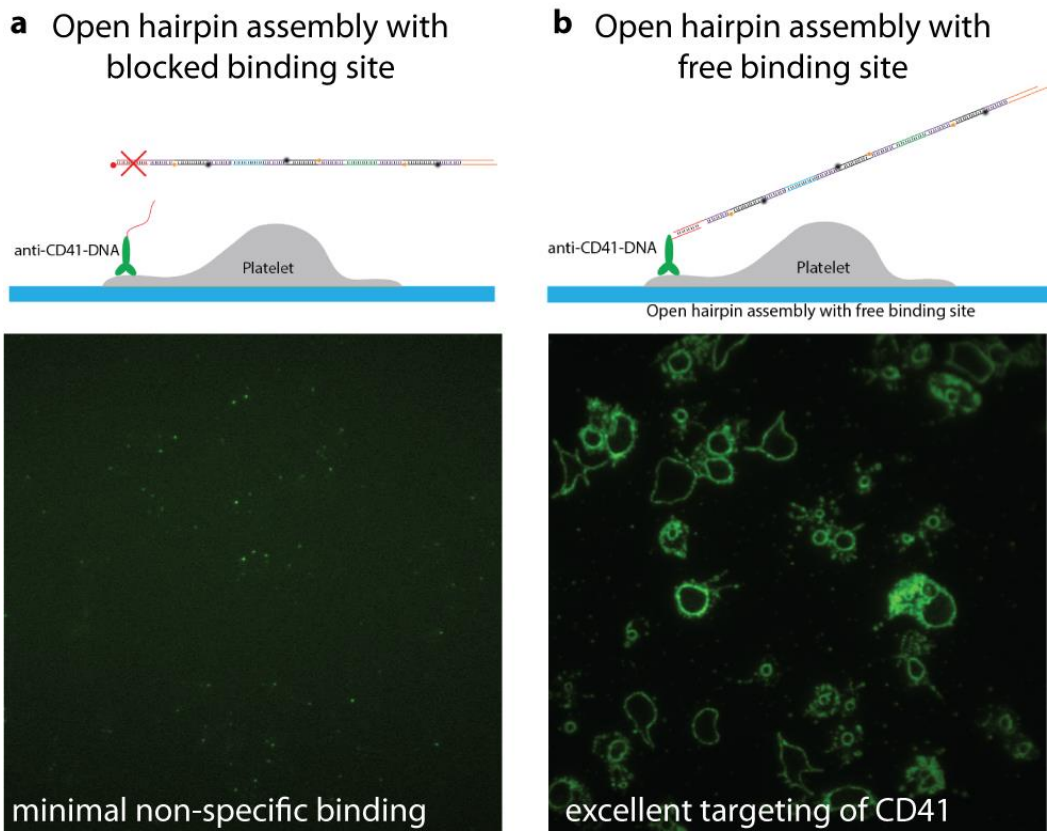

Figure 45 *- We have successfully conjugated DNA based fluorescent reporters onto anti-CD41 and shown (a) minimal non-specific binding and (b) highly specific platelets targeting.*

We sought to determine if our nanoreporters could target specific cell markers. We focused our initial experiments on platelets given our collaborators' extensive experience [39, 47-54] obtaining and using platelets. We conjugated a DNA oligo with sequence identical to the current digoxigenin strand to anti-CD41 using SoluLink® Protein-Oligo Conjugation Kit. Substitution of digoxigenin with this antibody-DNA conjugate switches the targeted binding site from anti-digoxigenin to platelet-specific integrin $\alpha_{IIb}\beta_3$, and is abundantly expressed on the platelet surface. Proper activity of the antibody after conjugation with DNA was first verified. Platelets were isolated using standard protocols and plated in a simple microfluidic structure created from PDMS

channels (40mm x 2mm x 100um) and a No. 1.5 coverslip. The platelets were coated with the FPLC purified anti-CD41-DNA then washed with tween-20-free buffer. We incubated the platelets with constitutively open 10-hairpin-chains with either free or blocked anti-CD41-DNA hybridization sites. The hairpin chains with blocked hybridization sites showed very low binding, while the hairpin chains with free binding sites demonstrated excellent binding and fluorescence (Figure 45). Images were taken with TIRF so only the edges of the platelets are clearly visible – thicker areas of the platelets cannot be visualized with TIRF.

Following these results, we attempted to assemble and use shear to activate the complete nanoreporter on platelets. Purified hairpin-tether assemblies were incubated on beads as done previously, but without the anti-CD41-DNA. Following a washing

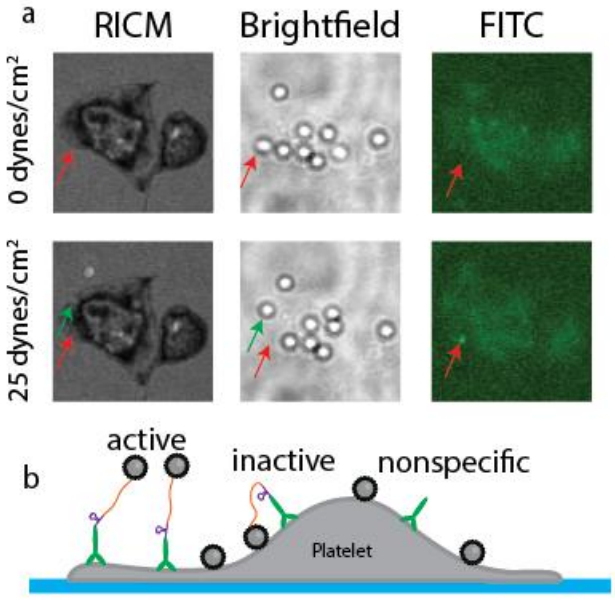

Figure 46 *- We have successfully conjugated DNA based fluorescent reporters onto anti-CD41 and shown (a) shear flow mediated activation of nanoreporter on platelet surface. Red arrows indicate bead of interest initial location, green arrows indicate post-flow location. (b) Schematic of suspected bead populations, with more nonspecific and inactive beads.*

step of the platelets using 1%BSA PBS buffer, the platelets were then incubated with a high concentration of anti-CD41-DNA and washed again. Finally, the hairpin-tether-bead assembly was incubated on the prepared platelets shortly before imaging.

One key concern is that the applied forces will alter the binding affinity of the antibodies and that they will be unable to attach to the surface of the cells under flow. However, based on previous literature demonstrating that antibodies with nanomolar equilibrium constants may have disassociation forces on the order of 40 – 160nN [55], which is more than an order of magnitude higher than the typical hairpin forces required for fluorescence. Our preliminary data suggest that this is not a concern for CD41 on platelets as the nanoreporter fluoresces at 25 dynes/cm^2 (**Figure 46a**). With an active sensor yield of at best 5%, we noted significant non-specific binding from the streptavidin coated beads, which is not unexpected given previous experience that beads stick to any biological materials present on the glass. This nonspecific binding could also be attributed to an RYD sequence expressed by wild type streptavidin that mimics RGD (Arg-Gly-Asp). RGD is the universal recognition domain present in fibronectin and other adhesion-related molecules [56]. Based on this, we will reduce adhesion by passivating the bead surface by saturating unbound streptavidin with biotinylated PEG at least 1 kD in size. Another option is to coat a bead in mutated streptavidin that does not contain this RYD sequence.

Future Work – Test Nanoreporter in Endothelialized Microfluidics

We will work to identify and test a series of sensors designed to target various antigens starting with endothelial cell markers CD31/PECAM, VCAM, and CD43. Similar to how

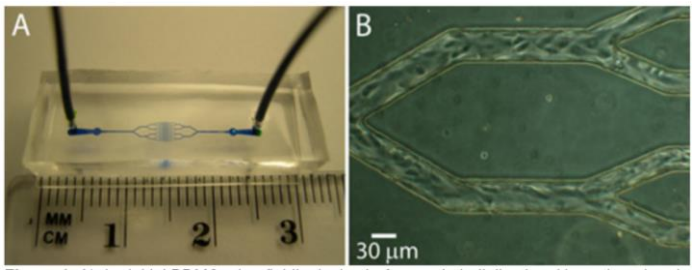

Figure 47 - *Endothelialized microfluidics represent an ideal testbed for the nanoreporter by recapitulating essential features of a blood vessel while also providing exceptional control over shear.*

we confirmed that targeting was viable with our custom conjugated CD41-DNA, we will perform all preliminary binding and fluorescence verification with the new cell marker targets. Also, we may test binding under flow conditions, which we have not done yet for preliminary experiments.

We will next examine the nanoreporter performance in a well-controlled microphysiological system. Dr. Myers has extensive experience in designing, culturing, and maintaining “endothelialized microfluidics” [41, 43, 51, 57]. Both microfluidic [41, 43, 51] and larger “microfluidics” [57] can be coated in a 3D conformal layer of endothelial cells that recapitulates the essential features of a biological system. At the same time, this approach provides unprecedented control over the fluidic shear stress that could not be achieved *in vivo*. Here, we will use this system by conjugating various antibodies to the previously characterized endothelial targets (CD31, VCAM, CD43, $\alpha_4\beta_1$). Both small microfluidics and large macrofluidics will be utilized to test a range of shear stresses and sensors from 0 – 10,000 dynes/cm^2. The goal of this work will be to optimize a delivery strategy, to compare the performance and consistency of nanoreporters to various antigen targets. We will characterize the amount of binding for each target for a specific concentration of nanoreporter and compare this number

to the number of possible binding sites on the endothelium to calculate a binding performance. Initial testing will be performed on systems perfused with saline buffer to facilitate testing. As many of the potential application areas feature simple cell-free biofluids interfacing with a cell surface, data on binding efficiency will provide insights into other systems. However, as shear testing in blood also represents an area of key importance, we will repeat this testing using whole blood. A key objective will be identifying how the presence of cells in the biofluid influences the behavior of the shear nanoreporters.

Conclusion

So far we have demonstrated a nanoreporter that reliably and repeatably produces a fluorescent output signal in response to application of fluidic shear. We have plans to further explore and expand the capability of this system in terms of shear detection threshold, more robust nanoreporter design, and multiplexed imaging. Additionally, we believe that a DNA-only biological reporter can be designed and verified, and that these reporters can be targeted to and are functional on cell types physiologically relevant to diseases of interest.

References

1. Watson, J.D. and F.H.C. Crick, *Molecular Structure of Nucleic Acids: A Structure for Deoxyribose Nucleic Acid.* Nature, 1953. **171**(4356): p. 737-738.
2. Cui, S., Y. Yu, and Z. Lin, *Modeling single chain elasticity of single-stranded DNA: A comparison of three models.* Polymer, 2009. **50**(3): p. 930-935.
3. Winfree, E., et al., *Design and self-assembly of two-dimensional DNA crystals.* Nature, 1998. **394**(6693): p. 539-544.
4. Seeman, N.C., *Nucleic acid junctions and lattices*. Journal of Theoretical Biology, 1982. **99**(2): p. 237-247.
5. Wei, B., M.J. Dai, and P. Yin, *Complex shapes self-assembled from single-stranded DNA tiles.* Nature, 2012. **485**(7400): p. 623-+.
6. Ke, Y.G., et al., *Three-Dimensional Structures Self-Assembled from DNA Bricks.* Science, 2012. **338**(6111): p. 1177-1183.
7. Rothemund, P.W., *Folding DNA to create nanoscale shapes and patterns.* Nature, 2006. **440**(7082): p. 297-302.
8. Rothemund, P.W.K., *Folding DNA to create nanoscale shapes and patterns.* Nature, 2006. **440**(7082): p. 297-302.
9. Douglas, S.M., et al., *Self-assembly of DNA into nanoscale three-dimensional shapes.* Nature, 2009. **459**(7245): p. 414-418.
10. Andersen, E.S., et al., *Self-assembly of a nanoscale DNA box with a controllable lid.* Nature, 2009. **459**(7243): p. 73-76.
11. Dietz, H., S.M. Douglas, and W.M. Shih, *Folding DNA into twisted and curved nanoscale shapes.* Science, 2009. **325**(5941): p. 725-730.
12. Han, D., et al., *DNA origami with complex curvatures in three-dimensional space.* Science, 2011. **332**(6027): p. 342-346.
13. Ke, Y.G., et al., *Multilayer DNA Origami Packed on Hexagonal and Hybrid Lattices.* Journal of the American Chemical Society, 2012. **134**(3): p. 1770-1774.
14. Gerling, T., et al., *Dynamic DNA devices and assemblies formed by shape-complementary, non–base pairing 3D components.* Science, 2015. **347**(6229): p. 1446-1452.
15. Benson, E., et al., *DNA rendering of polyhedral meshes at the nanoscale.* Nature, 2015. **523**(7561): p. 441-444.
16. Geary, C., P.W.K. Rothemund, and E.S. Andersen, *A single-stranded architecture for cotranscriptional folding of RNA nanostructures.* Science, 2014. **345**(6198): p. 799-804.
17. Veneziano, R., et al., *Designer nanoscale DNA assemblies programmed from the top down.* Science, 2016.
18. Han, D., *DNA gridiron nanostructures based on four-arm junctions.* Science, 2013. **339**(6126): p. 1412-1415.
19. Kuzyk, A., et al., *DNA-based self-assembly of chiral plasmonic nanostructures with tailored optical response.* Nature, 2012. **483**(7389): p. 311-314.
20. Wang, P., et al., *Visualization of the Cellular Uptake and Trafficking of DNA Origami Nanostructures in Cancer Cells.* Journal of the American Chemical Society, 2018. **140**(7):

p. 2478-2484.
21. Brockman, J.M., et al., *Mapping the 3D orientation of piconewton integrin traction forces.* Nature Methods, 2018. **15**(2): p. 115-118.
22. Li, Y., Y.T.H. Cu, and D. Luo, *Multiplexed detection of pathogen DNA with DNA-based fluorescence nanobarcodes.* Nature Biotechnology, 2005. **23**: p. 885.
23. Levsky, J.M., et al., *Single-Cell Gene Expression Profiling.* Science, 2002. **297**(5582): p. 836.
24. Geiss, G.K., et al., *Direct multiplexed measurement of gene expression with color-coded probe pairs.* Nat Biotechnol, 2008. **26**(3): p. 317-25.
25. Lin, C., et al., *Submicrometre geometrically encoded fluorescent barcodes self-assembled from DNA.* Nat Chem, 2012. **4**(10): p. 832-9.
26. Wagenbauer, K.F., C.H. Wachauf, and H. Dietz, *Quantifying quality in DNA self-assembly.* Nature Communications, 2014. **5**(1): p. 3691.
27. Douglas, S.M., et al., *Rapid prototyping of 3D DNA-origami shapes with caDNAno.* Nucleic Acids Research, 2009. **37**(15): p. 5001-5006.
28. Huppa, J.B., et al., *TCR–peptide–MHC interactions in situ show accelerated kinetics and increased affinity.* Nature, 2010. **463**(7283): p. 963-967.
29. Chen, W., et al., *Measuring Receptor–Ligand Binding Kinetics on Cell Surfaces: From Adhesion Frequency to Thermal Fluctuation Methods.* Cellular and Molecular Bioengineering, 2008. **1**(4): p. 276.
30. Kanner, S.B. and O.K. Haffar, *HIV-1 down-regulates CD4 costimulation of TCR/CD3-directed tyrosine phosphorylation through CD4/p56lck dissociation.* The Journal of Immunology, 1995. **154**(6): p. 2996.
31. Yin, Y., X.X. Wang, and R.A. Mariuzza, *Crystal structure of a complete ternary complex of T-cell receptor, peptide–MHC, and CD4.* Proceedings of the National Academy of Sciences, 2012. **109**(14): p. 5405.
32. Dutta, P.K., et al., *Programmable Multivalent DNA-Origami Tension Probes for Reporting Cellular Traction Forces.* Nano Lett, 2018. **18**(8): p. 4803-4811.
33. Chiu, J.J. and S. Chien, *Effects of disturbed flow on vascular endothelium: pathophysiological basis and clinical perspectives.* Physiol Rev, 2011. **91**(1): p. 327-87.
34. Maas, A.H.E.M., et al., *Microvascular Angina: Diagnosis, Assessment, and Treatment.* EMJ int Cardiol, 2019. **7**: p. 2-17.
35. Blanchard, A.T. and K. Salaita, *Emerging uses of DNA mechanical devices.* Science, 2019. **365**(6458): p. 1080-1081.
36. Nir, G., et al., *The role of near-wall drag effects in the dynamics of tethered DNA under shear flow.* Soft Matter, 2018. **14**(12): p. 2219-2226.
37. Santangelo, P.J., et al., *Single molecule-sensitive probes for imaging RNA in live cells.* Nat Methods, 2009. **6**(5): p. 347-9.
38. Zhang, Y., et al., *DNA-based digital tension probes reveal integrin forces during early cell adhesion.* Nature Communications, 2014. **5**(1): p. 5167.
39. Myers, D.R., et al., *Single-platelet nanomechanics measured by high-throughput cytometry.* Nature materials, 2017. **16**(2): p. 230-235.
40. Fay, M.E., et al., *Cellular softening mediates leukocyte demargination and trafficking, thereby increasing clinical blood counts.* Proceedings of the National Academy of

Sciences, 2016. **113**(8): p. 1987--1992.
41. Myers, D.R., et al., *Endothelialized Microfluidics for Studying Microvascular Interactions in Hematologic Diseases.* JoVE, 2012(64): p. e3958.
42. Winterton, J.D., et al., *A novel continuous microfluidic reactor design for the controlled production of high-quality semiconductor nanocrystals.* Journal of Nanoparticle Research, 2008. **10**(6): p. 893--905.
43. Sakurai, Y., et al., *A microengineered vascularized bleeding model that integrates the principal components of hemostasis.* Nature Communications, 2018. **9**(1): p. 509.
44. Fu, H., et al., *Flow-induced elongation of von Willebrand factor precedes tension-dependent activation.* Nat Commun, 2017. **8**(1): p. 324.
45. Perkins, T., et al., *Stretching of a single tethered polymer in a uniform flow.* Science, 1995. **268**(5207): p. 83-87.
46. Ley, K. and Y. Huo, *VCAM-1 is critical in atherosclerosis.* The Journal of Clinical Investigation, 2001. **107**(10): p. 1209-1210.
47. Williams, E.K., et al., *Feeling the Force: Measurements of Platelet Contraction and Their Diagnostic Implications.* Seminars in Thrombosis and Hemostasis, 2018.
48. Hansen, C.E., et al., *Platelet–Microcapsule Hybrids Leverage Contractile Force for Targeted Delivery of Hemostatic Agents.* ACS Nano, 2017. **11**(6): p. 5579-5589.
49. Sakurai, Y., et al., *Platelet geometry sensing spatially regulates $α$-granule secretion to enable matrix self-deposition.* Blood, 2015. **126**(4): p. 531--538.
50. Qiu, Y., et al., *Platelets and physics: How platelets "feel" and respond to their mechanical microenvironment.* Blood reviews, 2015. **29**(6): p. 377--386.
51. Ciciliano, J.C., et al., *Resolving the multifaceted mechanisms of the ferric chloride thrombosis model using an interdisciplinary microfluidic approach.* Blood, 2015. **126**(6): p. 817--824.
52. Qiu, Y., et al., *Platelet mechanosensing of substrate stiffness during clot formation mediates adhesion, spreading, and activation.* Proceedings of the National Academy of Sciences of the United States of America, 2014. **111**(40): p. 14430-14435.
53. Liu, F., et al., *Mitochondrially mediated integrin $α$IIb$β$3 protein inactivation limits thrombus growth.* Journal of Biological Chemistry, 2013. **288**(42): p. 30672--30681.
54. Chen, Y., et al., *Loss of the F-BAR protein CIP4 reduces platelet production by impairing membrane-cytoskeleton remodeling.* Blood, 2013. **122**(10): p. 1695--1706.
55. Schwesinger, F., et al., *Unbinding forces of single antibody-antigen complexes correlate with their thermal dissociation rates.* Proceedings of the National Academy of Sciences, 2000. **97**(18): p. 9972-9977.
56. Alon, R., E.A. Bayer, and M. Wilchek, *Streptavidin contains an RYD sequence which mimics the RGD receptor domain of fibronectin.* Biochemical and Biophysical Research Communications, 1990. **170**(3): p. 1236-1241.
57. Mannino, R.G., et al., *Do-it-yourself in vitro vasculature that recapitulates in vivo geometries for investigating endothelial-blood cell interactions.* Scientific reports, 2015. **5**.